Paleoceanography and Paleoclimatology

RESEARCH ARTICLE
10.1029/2023PA004685

High Productivity at High Latitudes? Photosynthesis and Leaf Ecophysiology in Arctic Forests of the Eocene

Wilfried Konrad[1,2], Anita Roth-Nebelsick[3], and Christopher Traiser[1]

[1]Department of Geosciences, University of Tübingen, Tübingen, Germany, [2]Technical University Dresden, Institute of Botany, Dresden, Germany, [3]State Museum of Natural History Stuttgart, Stuttgart, Germany

Key Points:

- Lush forests thrived in the Arctic during the Eocene under non-analogous climatic conditions
- Tree productivity of Eocene forests was studied for two exemplary fossil Arctic sites based on a photosynthesis model
- Compared to extant deciduous forests, productivity of Arctic Eocene forests was in the range of modern tropical forests

Correspondence to:
W. Konrad,
wilfried.konrad@uni-tuebingen.de

Citation:
Konrad, W., Roth-Nebelsick, A., & Traiser, C. (2023). High productivity at high latitudes? photosynthesis and leaf ecophysiology in Arctic forests of the Eocene. *Paleoceanography and Paleoclimatology*, *38*, e2023PA004685. https://doi.org/10.1029/2023PA004685

Received 22 MAY 2023
Accepted 3 AUG 2023

Author Contributions:
Conceptualization: Wilfried Konrad, Anita Roth-Nebelsick, Christopher Traiser
Formal analysis: Wilfried Konrad
Investigation: Anita Roth-Nebelsick
Methodology: Wilfried Konrad, Anita Roth-Nebelsick
Resources: Christopher Traiser
Software: Wilfried Konrad
Writing – original draft: Wilfried Konrad, Anita Roth-Nebelsick
Writing – review & editing: Wilfried Konrad, Anita Roth-Nebelsick

Abstract The Arctic forests of the Eocene, which thrived under elevated CO_2, a temperate climate, high precipitation and annually extremely different daylengths, represent a quite spectacular no-analogue habitat of Earth's greenhouse past. The aim of this study was to improve our understanding of the ecophysiology of Arctic broad-leaved deciduous forests of the Eocene, by analyzing leaf photosynthesis and tree productivity based on gas exchange modeling for two fossil Eocene sites, Svalbard and Ellesmere Island. For this, a single-leaf photosynthesis model that includes heat transfer and leaf senescence was derived. Environmental conditions were based on available palaeoclimate data and a CO_2 level of 800 µmol/mol. Additionally, different light regimes (diffusivity and transmissivity) were considered. With this model, annual photosynthesis was calculated on the basis of annual temperature and day lengths (derived by celestial mechanics). To obtain productivity of a whole deciduous broad-leaved tree, the single leaf data were then upscaled by a canopy model. The results indicate that productivity was enhanced at both high latitude sites by elevated CO_2, temperature of the growing season and high maximum daylength (24 hr) during late spring and early summer. With productivity values about 30%–60% higher as for a mid-latitude continental European forest, the results indicate a potential for high productivity at the Eocene polar sites which is in the range of extant tropical forests. In contrast to speculations, no evidence for a selective advantage of large leaf size—as shown by various fossil leaves from high latitude sites—could be found.

Plain Language Summary Greenhouse conditions of the past allowed forests to thrive in the Arctic. The productivity of early Eocene broad-leaved trees, growing about 55–45 million years ago within the Arctic circle, was studied by applying physiological models to the climate conditions of the past. The Arctic environment during that time was non-analogous, meaning that today there is no spot on Earth showing the same conditions which included a temperate climate, ample precipitation, 24 hr of daylight during early summer and a CO_2 concentration twice as high as today's CO_2 concentration. It was found that under these conditions, tree productivity is up to about 30%–60% higher as that of an extant temperate mid-latitude forest. Knowledge on the ecology of high-latitude environments of past greenhouse periods can provide valuable information for possible climate change scenarios of the future.

1. Introduction and Aims

One of the most striking aspects of the greenhouse climate of the past is the existence of polar forests which covered large regions in high latitudes well into the Eocene, with historical reports of fossil Arctic forests dating back to the nineteenth century (Budantsev, 1983; Collinson & Hooker, 2003; Heer, 1868; McIver & Basinger, 1999; Nathorst, 1915; Schei, 1903). Our knowledge on Arctic palaeoclimate is based to a large degree on Arctic fossil floras (Basinger et al., 1994; Greenwood et al., 2010; Jahren & Sternberg, 2003; Sunderlin et al., 2011; Uhl et al., 2007; West et al., 2015; Willard et al., 2019; Williams et al., 2008). For the Eocene Arctic, various studies provide evidence for mesothermal conditions with quite mild winters and ample precipitation (Eberle & Greenwood, 2012; Eldrett et al., 2009; Greenwood et al., 2010; West et al., 2015, 2020). The temperate and humid conditions allowed for a rich and lush Arctic vegetation before global cooling started to set in during the late Paleogene and the taxonomic richness and composition of high latitude forests and their changes through time are described in various studies (Eberle & Greenwood, 2012; Harrison et al., 2012; Kvaček et al., 1994; McIver & Basinger, 1999; West et al., 2019). Eocene Arctic forests were composed of a mix of both evergreen and deciduous conifers as well as deciduous angiosperms (Greenwood & Basinger, 1994; Kotyk et al., 2003; LePage, 2001, 2003; West et al., 2019; Willard et al., 2019). Also broad-leaved deciduous forests

were wide-spread (West et al., 2015 and citations therein). The fossil record of the Arctic forests comprises in situ fossil tree trunks which indicate high tree height and density (Francis, 1988, 1991; Williams et al., 2003).

The polar regions of the Eocene were no-analogue habitats, featuring special conditions which cannot be found today (West et al., 2015). In view of global climate change, no-analogue habitats of the past are receiving increasing attention due to the challenges posed for ecological forecasting: Ongoing changes lead to environments for which no extant counterpart exists but analogue conditions can be found in the past (Burke et al., 2018). High-latitude environments of the Eocene greenhouse period provide valuable information on possible ecological scenarios for regions which may change rapidly in the future. During the Eocene, the high latitudes featured a combination of moderate temperatures and substantially elevated atmospheric carbon dioxide concentration (C_a) with extremely different daylight lengths during a year, from 24 hr daylight in summer to permanent darkness for part of the winter. Photosynthesis was not possible during the lightless winter period, leading to a "photic seasonality" (West et al., 2015).

In various studies, possible ecological and ecophysiological consequences of these special conditions were addressed. From the tree trunk remains of a fossil forest in Ellesmere Island, which was dominated by the deciduous conifer *Metasequoia*, Williams et al. (2008) estimated a primary productivity per area and year similar to the productivity of extant forests of the Pacific Northwest and temperate flood plain forests in North America. Based on extant correlations between leaf size data and primary productivity data, Reichgelt et al. (2022) concluded that high-latitude sites on the Southern Hemisphere could have reached a productivity of possibly more than 1,000 g C/m^2/a.

Many fossil angiosperm leaves from fossil polar forests show quite large laminas. For instance, West et al. (2015) reported that a large part of morphotypes of Stenkul Fiord were assigned to three large leaf size categories of CLAMP (leaf area classes between 40 and 100 cm^2). Such large leaves signal wet conditions, which is mainly supported by other sources of palaeoclimate information (West et al., 2015). It was also suggested that a high proportion of diffuse light, mainly caused by dense cloud cover, additionally promoted larger leaves in angiosperms (West et al., 2015).

A detailed analysis of leaf function and productivity in the deciduous angiosperms thriving under the non-analogous conditions of the Eocene Arctic is, however, lacking so far. This study sets out to improve our understanding of the ecology of Arctic broad-leaved angiosperms, by analyzing leaf ecophysiology under conditions of Eocene climate and high latitude insolation. For this purpose, two well-studied polar Eocene fossil sites were selected: Ellesmere Island (Northern Canada) and the Svalbard archipelago around Spitsbergen (Norway). For these sites, comprehensive reconstructions of palaeoclimate are also available. For comparison, a mid-latitude continental European site will also be considered whose modern climate is very similar to that of the Eocene Arctic sites.

In detail, the aims of the present study are to:

1. model photosynthesis and transpiration for deciduous broad leaves in Arctic forests under Eocene climate and CO_2 conditions,
2. evaluate the impact of leaf size,
3. calculate whole-tree primary productivity.

2. Fossil Sites

2.1. Ellesmere Island

Various fossil sites are situated at Ellesmere island, providing outcrops rich in plant fossils from the Paleocene and Eocene (recently summarized and described by West et al. (2019)). For example, Stenkul Fiord, stratigraphically placed from the latest Paleocene to the Early Eocene (see West et al., 2015 and citations therein) features a fossil megaflora. The flora is composed of mixed conifer and broad-leaved angiosperms (McIver & Basinger, 1999, p. 531). The fossil site Stenkul Fiord is located on the southern shore of a fjord opening into the south-eastern part of Ellesmere Island (Canadian-Arctic Achipel) (Figure 1, Table 1). The Stenkul Fiord site contains remains of both plants and animals (Eberle & Greenwood, 2012; Harrington et al., 2011). U-Pb dating of the outcrops on the southern shore of Stenkul Fiord of the formation indicates an age of 52.6 Ma ± 1.9 Ma (Reinhardt et al., 2013). Together with dating from the vertebrate fauna, the flora of Stenkul Fiord can be

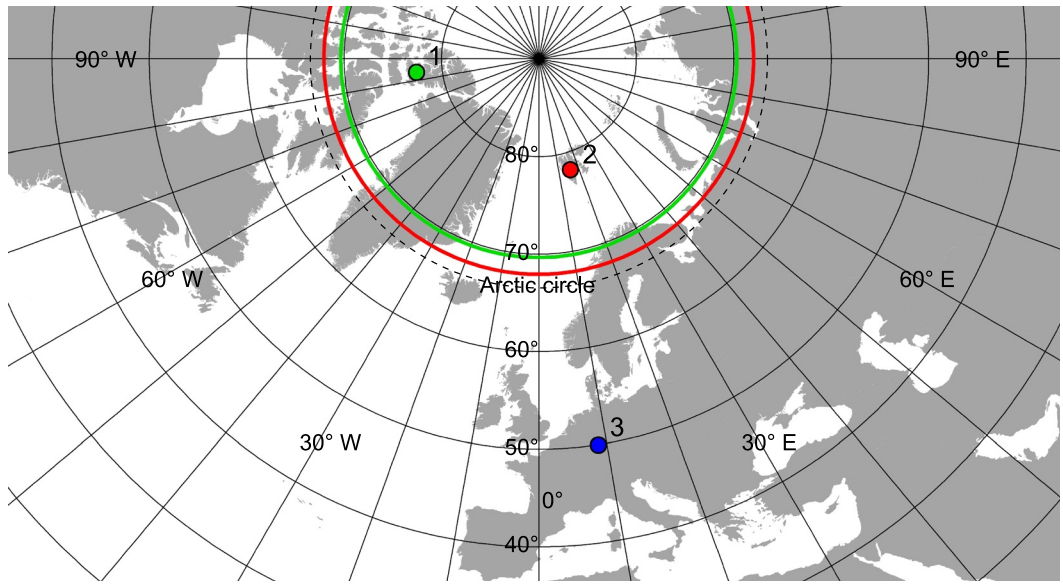

Figure 1. Palaeo-latitude of the two polar forest sites (circles of latitude) and their present day position (points): (1) Ellesmere Island (green), (2) Svalbard (red) and the position of the present-day mid-latitude site (3) near Darmstadt, Germany (blue).

stratigraphically placed as Early Eocene in age (West et al., 2015). Palaeo-climatic data of the flora based on nearest living relative analysis, leaf margin analysis and CLAMP are given by West et al. (2015) (see Table 1).

2.2. Svalbard

The Paleogene fossil record of Svalbard is dominated by plant fossils, vertebrate fauna records are very rare. An important stratigraphic element of the fossil record is the Aspelintoppen Formation, located in various outcrops in the southern part of Svalbard (Figure 1, Table 1), which represents a diverse angiosperm flora (Kvaček et al., 1994; Uhl et al., 2007; Wappler & Denk, 2011). The stratigraphic position is tentatively placed to the Lower Middle Eocene transition and corresponds to the middle part of the Aspelintoppen Formation (Crabaugh & Steel, 2004). Dinocysts, however, indicate an unresolved Eocene age (Manum & Throndsen, 1986). Radiometric stratigraphic data are so far not available. The "polar coal-forming and riparian deciduous forest" is characterized by mesophytic components including, amongst others, *Aesculus, Corylites, Craspedodromophyllum, Ginkgo* and *Ushia*, while *Metasequoia, Taxodium, Trochodendron* and Ulmaceae belong to the intrazonal part of the flora (Kvaček, 2010). Angiosperms are represented mainly by deciduous broad-leaved species showing leaves with thin texture which are on average of moderate size. Several species can have extremely large leaf blades up to 20–30 cm in diameter (Golovneva, 2000b). Palaeo-climatic data for Svalbard based on CLAMP are given by Golovneva (2000a, 2000b) and Uhl et al. (2007). The studies providing palaeo-climatic data for Aspelintoppen are mostly consistent, thus we refer here to data from Uhl et al. (2007) (see Table 1). In addition, the CLAMP results are consistent with the plant-taxon based reconstruction of Willard et al. (2019) for a site situated in the Arctic Basin.

2.3. Mid-Latitude Central-European Site (MMLS)

In order to compare the polar forests to a present-day mid latitude site (≈50°N) in Central Europe, an area at the north-western Odenwald (Hesse, Germany) was selected (Figure 1, Table 1). This region is characterized by ample broad leaved deciduous forests in an undulating foothill zone with an elevation between 150 and 350 m. This site, termed MMLS (modern mid-latitude site) in the following, was selected due to the similarity between its extant climate conditions and the Eocene climate of the Aspelintoppen formation of Svalbard. To evaluate the impact of CO_2, the MMLS model was additionally calculated with the CO_2 concentration of the Arctic sites (in what follows indicated as $MMLS_{elevated}$).

Table 1
(Palaeo-)Geographic, Climatic and Phenological Data for the Eocene (50 Ma) Polar Forests of Ellesmere Island, Svalbard, and the Modern Mid-Latitude Site (MMLS) Near Darmstadt, Germany

	Ellesmere Island	Svalbard	MMLS
(Palaeo-)geography[a]			
Modern longitude	83.59°W	15.64°E	8.75°E
Modern latitude	77.35°N	78.22°N	49.75°N
Palaeo latitude	69.70°N	67.94°N	—
Dating [Ma]	52.6 ± 1.9	Early Eocene	—
Climatic data[b]			
Number of morphotypes [*n*]	25	21	—
MAT [°C]	12.7	9.0	9.5
CMT [°C]	3.6	0.1	0.0
WMT [°C]	22.0	18.0	18.5
GSL [months]	7.5	5.4	5.8
GSP [mm]	904	357	361
w_{rel} [%]	84.0	79.1	77.3
Atmospheric CO_2 [µmol/mol]	800	800	415/800[d]
Number of polar days/nights per year [*n*]			
Polar nights with 0 sun hours	83	41	—
Transition days in first half of the year	100	142	—
Polar days with 24 sun hours	99	41	—
Transition days in second half of the year	83	141	—
Number of days per season [d][e]			
Winter	65	128	127
Springtime	41	33	33
Summer	218	170	173
Autumn	41	34	32
Sum of sun hours per season [h][c,e]			
Winter	152.7	565.4	1162.2
Springtime	441.6	483.5	434.9
Summer	3751.4	3116.9	2480.8
Autumn	37.6	217.3	303.2
Mean value of daily sun hours per season [h][c,e]			
Winter	2.3	4.4	9.2
Springtime	10.8	14.7	13.2
Summer	17.2	18.3	14.3
Autumn	0.9	6.4	9.5

Note. MAT, mean annual temperature; CMT, mean temperature of coldest month; WMT, mean temperature of warmest month; GSL, growing season length; representing the number of months with daily mean temperature $T_a > 10$°C, GSP: growing season precipitation, representing the sum of precipitation of months with mean temperature $T_a > 10$°C, w_{rel}: relative humidity of atmosphere.

[a]Data according to van Hinsbergen et al. (2015). For the Aspelintoppen Formation of Svalbard, the coordinates of Longyearbyen were selected. For Svalbard, no radiometric dating is available. [b]Climate data of the three Eocene sites are based on CLAMP analyses: Ellesmere Island (Stenkul Fiord: West et al. (2015)), Svalbard (Aspelintoppen Formation: Uhl et al. (2007)); data for the modern mid-latitude site have been calculated from New et al. (1999). [c]Sun hours are calculated under the assumptions of a cloudless sky and a spherical earth (i.e., no mountain ranges). [d]To evaluate the effect of CO_2, gas exchange at the MMLS will also be calculated with 800 µmol/mol. This model variation will be termed $MMLS_{elevated}$. [e]"Season" is to be understood in the phenological sense, as defined in Section 3.4 and shown in Figure 5.

2.4. Palaeo-Latitudes

Continental drift shifted the investigated fossil sites since the Paleogene. The paleo-latitudes of the sites were calculated with the palaeo-latitude model of van Hinsbergen et al. (2015) (http://www.paleolatitude.org) based on an approximative age of 50 Ma. The present day position of the sites as well their palaeo-latitude are shown in Figure 1 and Table 1.

3. Methods

3.1. Leaf Gas Exchange and Leaf Temperature

For modeling photosynthesis under polar Eocene conditions, we apply the model described in Konrad et al. (2017, 2020). It combines a model of leaf gas exchange (based on photosynthesis and the diffusion of water vapor and CO_2 through the stomatal openings) with the equation of leaf energy balance, thereby including the influence of leaf temperature on photosynthesis. Since there will be often a difference between air temperature and leaf temperature, particularly for larger leaves, integration of leaf temperature (which is dynamically interacting with cooling by transpiration) into the model when calculating photosynthesis is more realistic than to simply assume that leaves show air temperature. By calculating photosynthesis under leaf temperature conditions, it is therefore possible to include the effect of leaf size on leaf function. The model allows to calculate leaf temperature T_l, leaf conductance g, assimilation rate A, and transpiration rate E. For this, various input parameters are necessary which can be obtained from fossil leaves and palaeo-climate data. Additionally, biochemical parameters are necessary which have to be borrowed from suitable extant related taxa which can be considered to be ecological representatives.

The model is primarily based on two equations which are described in the following.

1. First, leaf conductance g is expressed in terms of the biochemical parameters q, Γ, K and R_d (see Table 2), defined in the model of photosynthesis (Farquhar et al., 1980, 2001) and the ratio $\kappa = C_i/C_a$ between leaf internal (C_i) and atmospheric (C_a) carbon dioxide concentration

$$g = \frac{q(\kappa C_a - \Gamma)}{(\kappa C_a + K)(1-\kappa)C_a} - \frac{R_d}{(1-\kappa)C_a} \tag{1}$$

The biochemical parameters depend on leaf temperature T_l (Bernacchi et al., 2003), implying that g is a function of T_l.

2. Second, leaf energy balance is calculated by

$$aI_l + a_{IR}\,\sigma\left(T_{surr}^4 + T_{sky}^4\right) \approx 2e_{IR}\,\sigma T_l^4 + \frac{2K_a}{d_{bl}}(T_l - T_a) + 2H_{vap}\,[w_l(T_l) - w_a]\bar{a}\,g(T_l) \tag{2}$$

(The variables in this equation are explained in Table 2). The terms on the left-hand side quantify the absorption of direct and diffuse shortwave radiation coming from the sun (first term), from the closer surroundings (such as other plants, second term) and of diffuse long wave radiation from the sky (third term). The right-hand side quantifies radiation emitted by the leaf (first term), heat exchange via conduction and convection (second term) and evaporative cooling by transpiration ($\bar{a} := D_{H_2O}/D_{CO_2}$ denotes the ratio of the molecular diffusional coefficients of water vapor and CO_2 in air, T_a is air temperature, and H_{vap} is the latent heat of vapourization). The conduction/convection term depends on the thickness d_{bl} of the laminar boundary layer attached to the leaf surface and on the free stream wind velocity v_w as well as the characteristic leaf length l_c. It reads (Nobel, 2005)

$$d_{bl} = 4 \times 10^{-3}\,(\mathrm{m}/\sqrt{\mathrm{s}})\,\sqrt{l_c/v_w} \tag{3}$$

(m and s denote the units meter and second, respectively). l_c is a kind of "averaged" streamwise leaf width and can be considered to represent leaf size (Schuepp, 1993). As expected, d_{bl} increases with increasing l_c and is reduced with increasing v_w. In this contribution, l_c will be systematically varied to grasp the leaf size variation at both fossil sites and to evaluate the influence of leaf size.

Table 2
The Model Parameters Together With Their Dimensions

Quantity [units]	Explanation	Value/remarks
Physiologic parameters		
A [μmol/m^2/s]	Assimilation rate	Output, Equation 5
A_{ann} [mol/m^2]	Annual assimilation per leaf area	Output, Figures 6 and 7
A_{tot} [kmol]	Annual whole tree assimilation	Equation D8, Table 3, Figure 9
E [mmol/m^2/s]	Transpiration rate	Output, Equation 6
E_{ann} [kmol/m^2]	Annual transpiration per leaf area	Output, Figures 6 and 7
E_{tot} [kmol]	Annual whole tree transpiration	Output, Table 3, Figure 10
g [m/s]	Leaf conductance	Internally calculated parameter
C_i [mol/m^3]	Leaf internal CO_2	Internally calculated parameter
T_l [°C]	Leaf temperature	Output, Figure 8
w_l [mol/m^3]	Leaf internal humidity	Equation 4
l_c [mm]	Characteristic leaf length	Input, Figure 6
Environmental parameters		
C_a [mol/m^3]	Atmospheric CO_2	Input, Figure 7
T_a [°C]	Air temperature	Input, Equation 8
w_{sat} [mol/m^3]	Saturation value of humidity	Equation 4
w_{rel} [−]	Relative atmospheric humidity	Input, Table 1
v_w [m/s]	Wind velocity	1.0
d_{bl} [mm]	Thickness of boundary layer	Equation 3
S_c [J/m^2/s]	Solar constant	1366
σ [J/m^2/s/K^4]	Stefan-Boltzmann constant	5.67×10^{-8}
K_a [J/m/s/K]	Coefficient of thermal conductivity of air at 20°C	2.55×10^{-2}
H_{vap} [J/mol]	Vaporization heat of water	44.1×10^3
Celestial mechanics and radiation		
ϑ	Angle of sun above horizon	Equation A1
τ [−]	Atmospheric transmissivity	Input, Figures 3, 6–8
k_d [−]	Diffuse fraction of solar radiation	Input, Figures 3, 6–8
a [−]	Absorptance of leaf for global radiation	≈0.60
r [−]	Reflectance of the surroundings for global radiation	≈0.20
a_{IR} [−]	Leaf absorptivity for infrared radiation	≈0.96
e_{IR} [−]	Leaf emissivity for infrared radiation	≈0.96
T_{surr} [°C]	Temperature of the surroundings	≈15
T_{sky} [°C]	Radiation temperature of the clear sky	≈−20
D_{CO_2} [m^2/s]	Diffusion constant of CO_2 at $T = 25$°C	1.55×10^{-5}
D_{H_2O} [m^2/s]	Diffusion constant of water vapor at $T = 25$°C	2.49×10^{-5}
$\bar{a}$ [−]	$\bar{a} := D_{H_2O}/D_{CO_2}$	1.6
Physiologic parameter values specific for *Cercidiphyllum japonicum*[a,b,c]		
q [μmol/m^2/s]	Carboxylation rate	Equation C3
K [μmol/m^3]	Photosynthetic parameter	Equation C6
Γ [μmol/m^3]	CO_2-compensation point in the absence of dark respiration	Equation C6
R_d [μmol/m^2/s]	Mitochondrial respiration rate	2.2
κ [−]	$\kappa := C_i/C_a$ = Leaf internal CO_2/Atmospheric CO_2	0.768
$J_{max,25°C}$	Maximum rate of electron transport at 25°C	58.38

Table 2
Continued

Quantity [units]	Explanation	Value/remarks
$V_{max,25°C}$	Maximum RuBP-saturated rate of carboxylation at 25°C	27.8
$R_{d,25°C}$	Mitochondrial respiration rate at 25°C	2.2
J [μmol/m^2/s]	Rate of electron transport	Equation C2
J_{max} [μmol/m^2/s]	Maximum rate of electron transport	Equation C6
K_o [mmol/mol]	Michaelis-Menten constant of oxygenation	Equation C6
K_c [μmol/mol]	Michaelis-Menten constant of carboxylation	Equation C6
p_o [mmol/mol]	Partial pressure of oxygen	Equation C6
Q [μmol/m^2/s]	Photosynthetic photon flux density	Equation C7
V_{max} [μmol/m^2/s]	Maximum RuBP-saturated rate of carboxylation	Equation C6
W_c [μmol/m^2/s]	Rubisco limited rate of carboxylation	Equation C1
W_j [μmol/m^2/s]	RuBP-limited rate of carboxylation	Equation C1
α_l [−]	Total leaf absorbance	0.9
β [−]	Fraction of absorbed quanta reaching PSII	0.66
Θ_{PSII} [−]	Convexity term for electron transport rates	Equation C6
$\Phi_{PSII,max}$ [−]	Maximum dark-adapted quantum yield of PSII	Equation C6
Further parameter values specific for *Cercidiphyllum japonicum*[d]		
h_c [m]	Height of tree crown	
r_c [m]	Radius of tree crown	
LAI [−]	Leaf area index	4.0
LAD [1/m]	Leaf area density	Equation D1
L_m [1/m]	Maximum value of LAD	0.53
z_m [m]	Height where LAD adopts the value L_m	0.3 h_c
k [−]	Extinction coefficient of Lambert-Beer law	0.4

Note. Numerical values represent constant parameters. Parameters designated as "input" are either varied (such as the characteristic leaf length) or differ between locations (climate parameters), in which case they are given in Table 1. Parameters designated as "output" are calculated by the model and provided in the results section or in the figures illustrating the model results. Various species-specific physiological parameters for the extant representative *Cercidiphyllum japonicum* are derived by equations as described in the table and in the footnotes.

[a]Values are taken from Kosugi et al. (2003). [b]κ is output from data given in Kosugi et al. (2003). [c]The temperature dependencies of the photosynthetic parameters are given in Equation C6. [d]Height and radius of tree crown are estimated on the basis of typical extant values for mesophytic temperate and deciduous trees, leaf are data are as in Lalic and Mihailovic (2004); Lalic et al. (2013).

The leaf internal humidity w_l, meaning absolute water content of a unit air volume, is close to its saturation value $w_{sat}(T_l)$ which depends on leaf temperature T_l. In a closed system at thermal equilibrium, w_l is provided by the Clausius-Clapeyron equation (Reif, 1974) as

$$w_l(T_l) \approx w_{sat}(T_l) = \frac{u}{T_l} \mathrm{e}^{\left(-\frac{v}{T_l}\right)} \tag{4}$$

with $u = 2.035 \times 10^{10}$ mol/m^3 and $v = 5{,}306$ (T_l in Kelvin).

Upon insertion of Equation 1 into Equation 2, a complex equation for leaf temperature T_l is obtained which can be solved using computational software (for this contribution the computer algebra system `maple` (Maplesoft, 2022) has been used). Once T_l is known, it can be used to obtain leaf conductance g (via Equation 1), assimilation rate

$$A = q\,\frac{\kappa C_a - \Gamma}{\kappa C_a + K} - R_d \tag{5}$$

and transpiration rate

$$E = g\bar{a}(w_l - w_a) \tag{6}$$

In order to employ the sequence of Equations 1–6 the quantity I_l in Equation 2 (representing the absorption of direct and diffuse shortwave radiation coming from the sun) has to be cast in a more explicit and tractable form. The result and its derivation is given in appendices Appendix A and Appendix B.

3.2. Required Parameters for Calculating Gas Exchange

All required input parameters for the model are listed in Table 2. These include physiological-biochemical parameters (such as q) as well as environmental parameters. Information on leaf size indicating ranges of characteristic leaf length l_c can be obtained from available data based on the fossil record (Uhl et al., 2007; West et al., 2015). Biochemical parameters have to be borrowed from ecologically representative relatives. *Cercidiphyllum japonicum*, belonging to the today monotypic family Cercidiphyllaceae, was selected due to its morphological and botanical affinity to the fossil leaves of *Trochodendroides* which was a common element of polar floras of Svalbard and Ellesmere Island (Uhl et al., 2007; West et al., 2019).

A crucial parameter for plant function is atmospheric concentration of CO_2. The range of reconstructed palaeo-CO_2 values for the Eocene, obtained by different methods, shows a quite high variation, and is still under debate. Results range from levels of about 600 µmol/mol to 700 µmol/mol (Foster et al., 2017; Jagniecki et al., 2015; Steinthorsdottir et al., 2019) to about 1,000 µmol/mol (Anagnostou et al., 2016) (see also https://www.paleo-co2.org/). Based on the discussed ranges of early Eocene CO_2, we assumed a value of 800 µmol/mol (see Table 2).

3.3. Required Environmental Parameters

Various environmental parameters are available from palaeoclimate results, such as CLAMP (Uhl et al., 2007; West et al., 2015) (summarized in Table 2) or from celestial mechanics. Highly relevant for analyzing ecophysiology of high latitude environments are parameters related to celestial mechanics, such as annual course of daylight length, because these differ greatly from conditions of middle and lower latitudes. These parameters and their derivation will be considered in the following sections and, in more detail, in Appendix A and Appendix B.

3.3.1. Length of Daylight

The time t_i of sunrise is calculated from setting $\vartheta = 0$ in Expression A1 (ϑ denotes the altitude of the sun above the horizon, η is the azimuth, Figure A1). Using $\eta = \omega t$ in Equation A1 (t is time of day and $\omega = 2\pi/(24\text{ hr})$) one obtains

$$t_i = \begin{cases} 12\,\text{h} \quad \text{(i.e. midday)} & \text{if } \tan\delta\tan\lambda < -1 \\ (1/\omega)\arccos(\tan\delta\tan\lambda) & \text{if } -1 \le \tan\delta\tan\lambda \le 1 \\ 0\,\text{h} \quad \text{(i.e. midnight)} & \text{if } \tan\delta\tan\lambda > 1 \end{cases} \tag{7}$$

λ denotes the latitude and δ the current declination, which depends—according to Equation A2—on d, the day of the year. Sunset occurs then at $t_f = 24\text{ hr} - t_i$ and length of day reads $t_{day} = t_f - t_i = 24\text{ hr} - 2\,t_i$.

3.3.2. Seasonal and Daily Temperatures

The annual temperature profiles of the fossil sites (Figure 2) were derived from the mean temperatures of the coldest month (CMT) and the warmest month (WMT)—they were calculated from the CLAMP data of Table 1—as follows: The annual variation of the daily mean temperature T_a as a function of the day of the year, d, is approximated by a sine function whose extrema represent CMT and WMT. The thermal inertia suggests that CMT and WMT lag 1 month behind winter and summer solstice, respectively.

$$T_a = \frac{\text{WMT} - \text{CMT}}{2}\sin\left[\frac{2\pi(d-81)}{365}\right] + \frac{\text{WMT} + \text{CMT}}{2} \tag{8}$$

The daily variation of temperature, T_d, is based on three assumptions: (a) the daily temperature maximum is 4 K warmer than the daily mean temperature T_a while the temperature minimum is 4 K cooler than T_a, (b) the

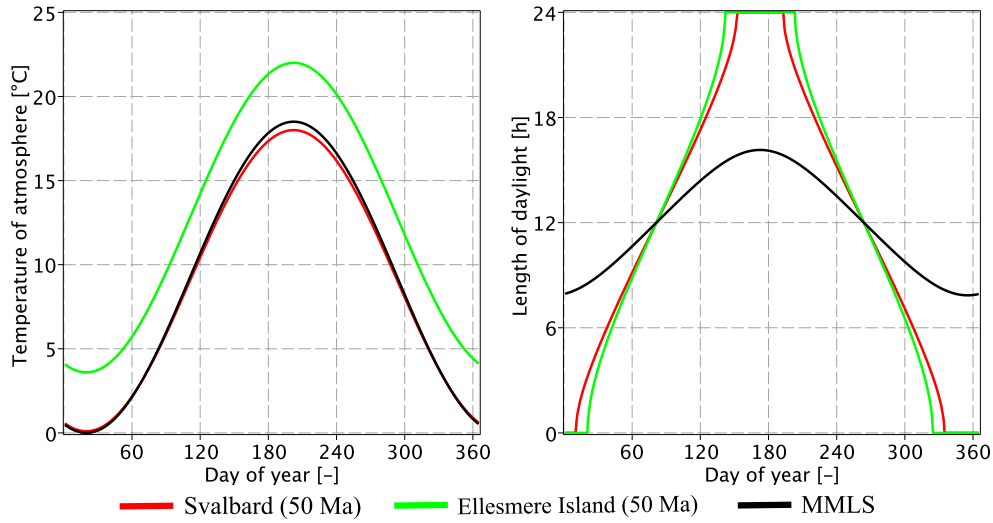

Figure 2. Variation of atmospheric mean temperature (left) and length of daylight (right) as a function of day of year for the locations Svalbard (latitude: $\lambda = 67.94°$N), Ellesmere Island ($\lambda = 69.70°$N), and the modern mid-latitude site (MMLS, $\lambda = 49.75°$N). Whereas annual course of temperature is almost identical for the MMLS and Svalbard, Ellesmere Island and Svalbard are similar with respect to daylight variation.

daily temperature maximum occurs at 13 hr and the temperature minimum occurs at dawn, that is, at time t_i (see Equation 7), and, (c) daily temperature variation with time occurs along sine functions whose extrema coincide with temperature minima and maxima.

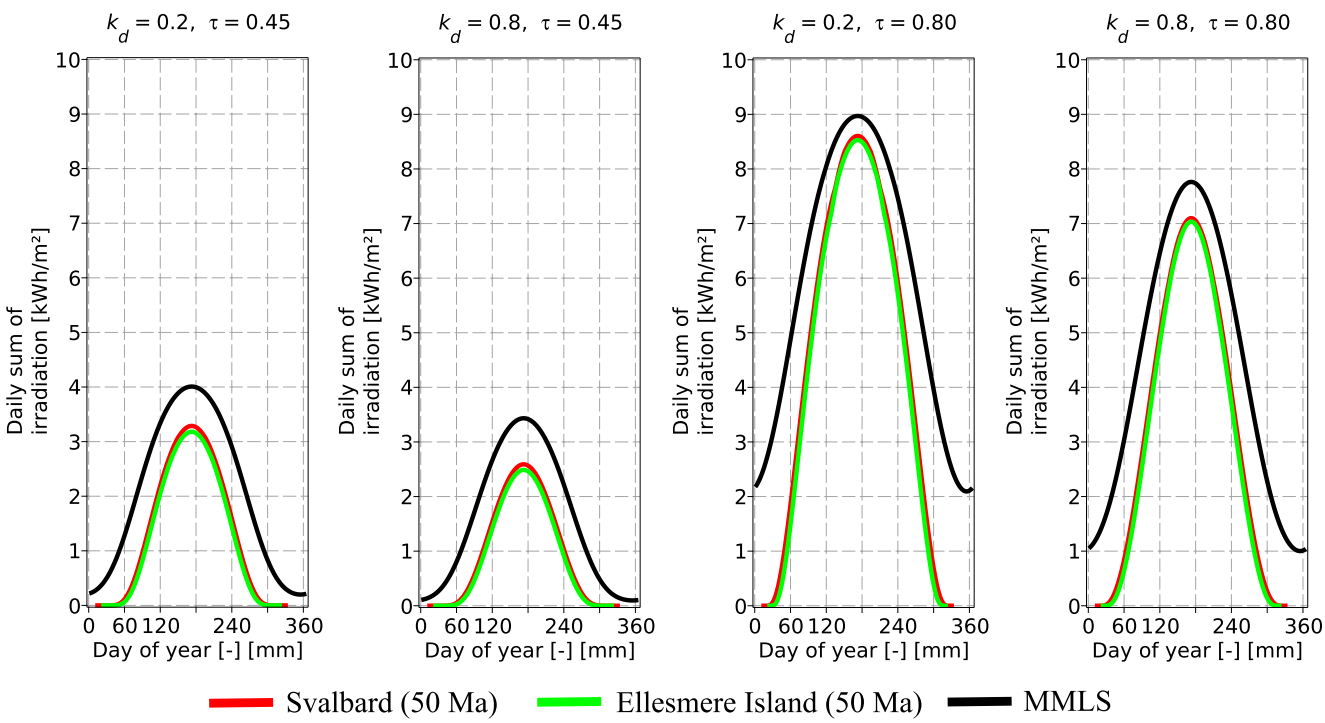

Figure 3. Daily sum of irradiation during growing season as a function of the day of the year for several combinations of the fraction of diffuse radiation k_d and atmospheric transmissivity τ. The leaf is oriented toward south and tilted by 45° against the horizontal.

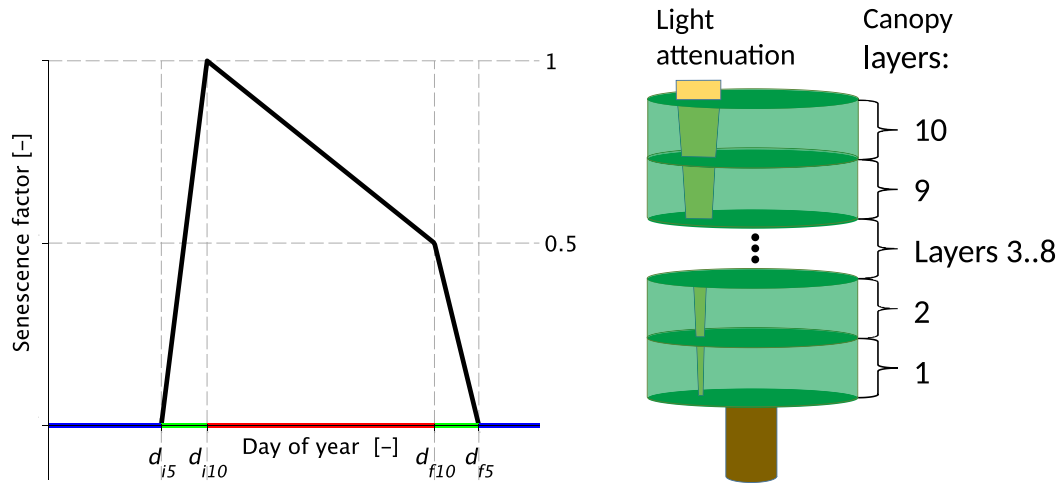

Figure 4. Left: Senescence factor (black curve) as a function of day of the year, according to Equation 9. The colors on the abscissa indicate the phenological phases winter (blue: $T_a < 5$°C), spring and autumn (green: 5°C < T_a < 10°C) and summer (red: $T_a > 10$°C). Right: A simple canopy model for a tree showing a height of 10 m and a crown radius of 4 m. The crown is shaped as a cylinder and it is composed of 10 circular segments. Each segment has a height of 1 m and a radius of 4 m.

3.3.3. Irradiation

The intensity of the solar radiation received by a leaf depends on (a) geographic latitude, time of day and day of year, (b) the orientation of the leaf with respect to the ground, and (c) on the optic properties of the atmosphere, especially atmospheric transmissivity τ and the fraction of diffuse light k_d (details can be found in Appendix A and Appendix B). This is illustrated by Figure 3.

3.4. Phenological Aspects

Based on (daily averaged) ranges of the air temperature T_a, we define four different phenological phases in the course of the year: (a) foliation (springtime), if 5°C < T_a < 10°C, (b) assimilation (summer, corresponding to "growing season" in CLAMP terminology), if $T_a > 10$°C, (c) leaf shedding (autumn), if 10°C > T_a > 5°C, and (d) leafless period for deciduous plants (winter), if $T_a < 5$°C and/or no insolation.

3.5. Senescence

Apart from their dependence on temperature and insolation, the photosynthetic parameters V_{max} and J_{max} (listed in Table 2, see also Appendix C) show also a seasonal variation called senescence (Hamada et al., 2016; Kikuzawa & Lechowicz, 2011; Wilson et al., 2000; Xu & Baldocchi, 2003). Typically, senescence leads to a reduction of V_{max} and J_{max} during the growing season from their maxima to about one-half of the maximum values. During (phenologically defined) spring—when leaves of deciduous trees unfold—photosynthetic capacity increases rapidly from zero to the maximum value, during autumn it decreases quickly to zero (Figure 4a).

To model these effects we define the "senescence factor"

$$S = \begin{cases} 0 & d < d_{i5} \\ \frac{d - d_{i5}}{d_{i10} - d_{i5}} & d < d_{i10} \\ \frac{2d_{f10} - d_{i10} - d}{2\left(d_{f10} - d_{i10}\right)} & d < d_{f10} \\ \frac{d - d_{f5}}{2\left(d_{f10} - d_{f5}\right)} & d < d_{f5} \\ 0 & d > d_{f5} \end{cases} \tag{9}$$

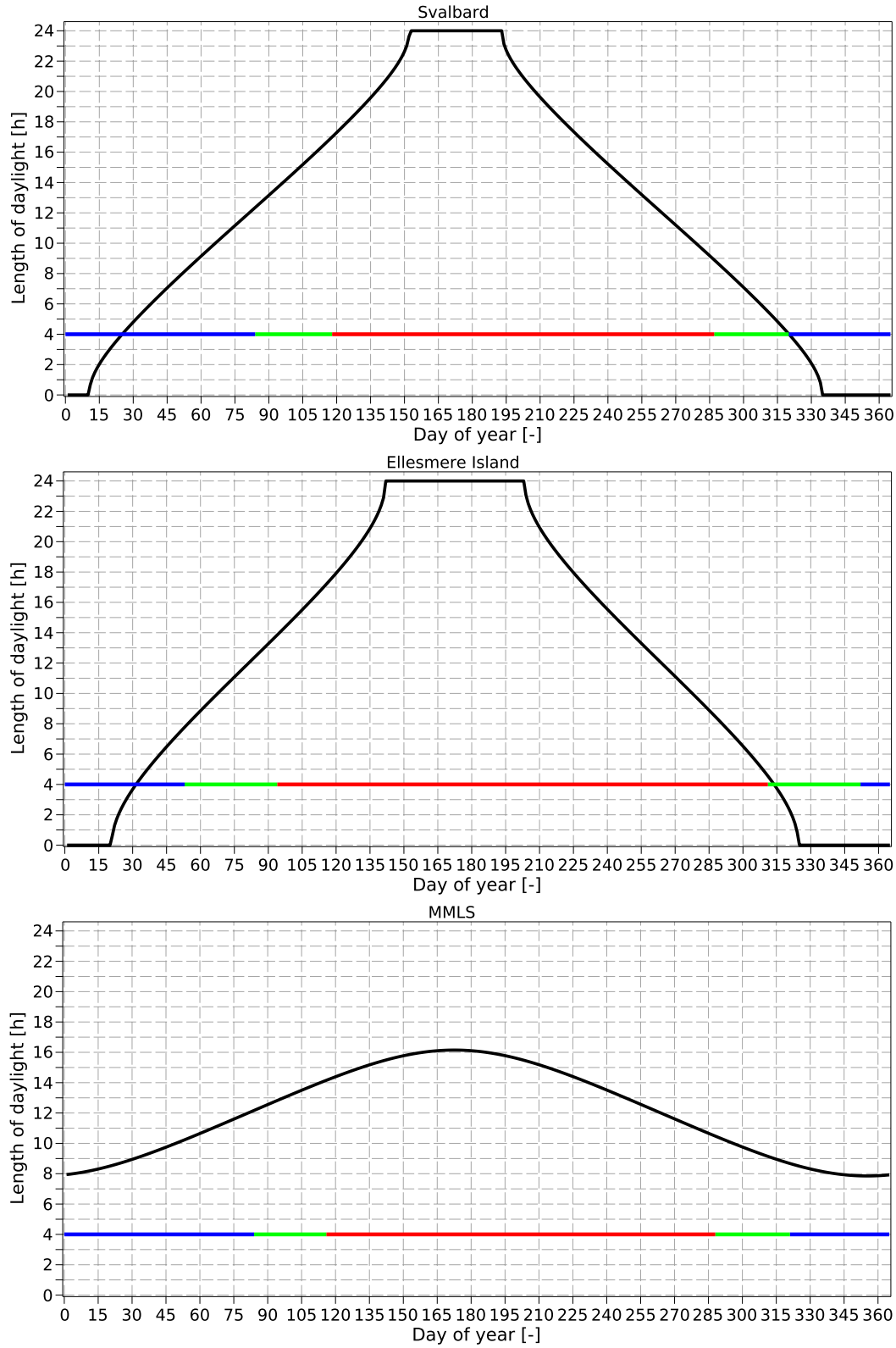

Figure 5. Length of daylight time (black curves) and averaged air temperature intervals (blue, green and red straight lines) of the sites Ellesmere Island (palaeolatitude: 69.70°N), Svalbard (palaeolatitude: 67.94°N) and MMLS (latitude: 49.75°N) as a function of day of year. Colors of air temperature are according to the phenologically defined seasons: Blue line: winter (T_a < 5°C), left green line: springtime (5°C < T_a < 10°C), red line: summer (T_a > 10°C), right green line: autumn (10°C > T_a > 5°C).

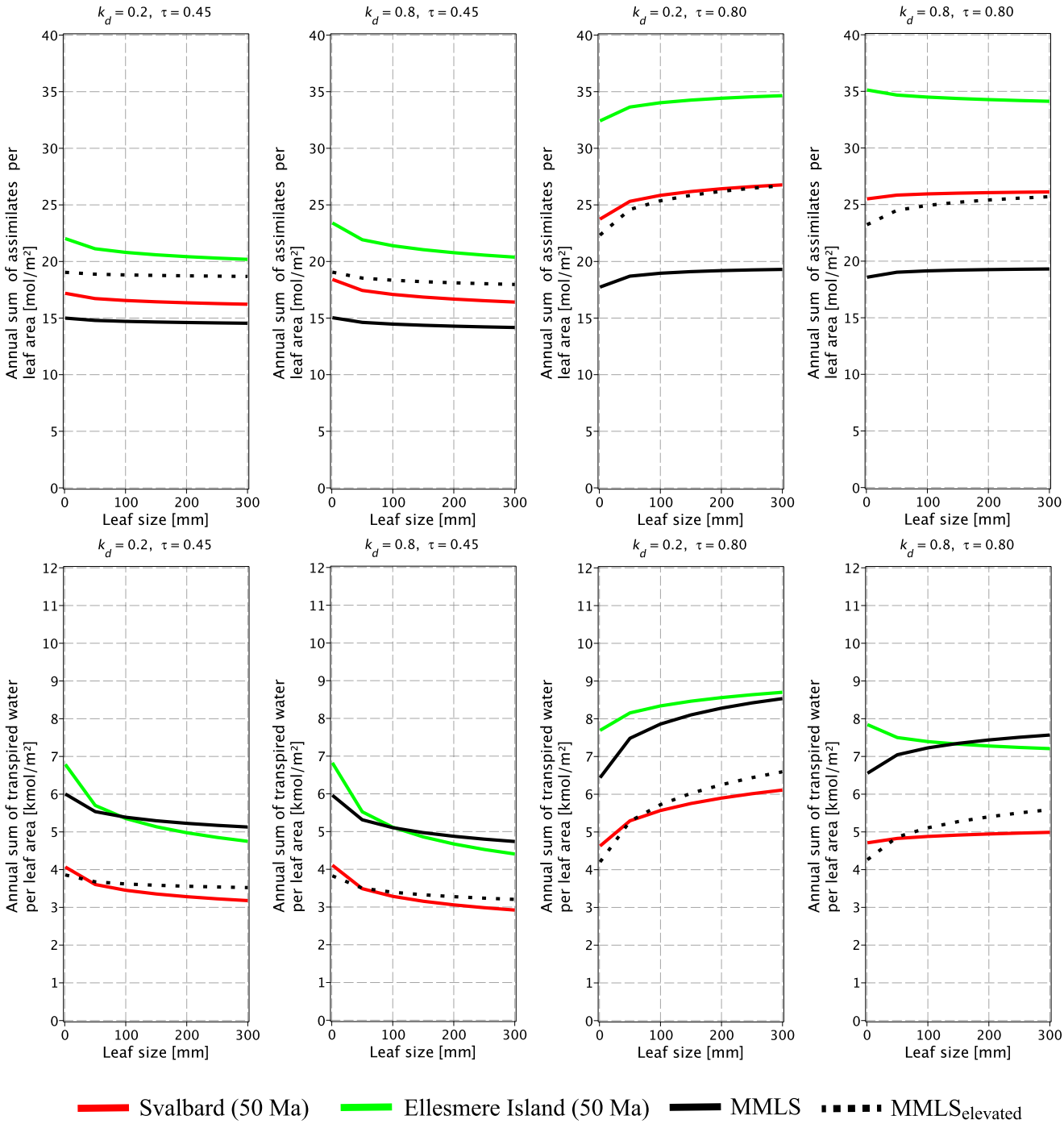

Figure 6. Annual assimilation A_{ann} (upper row) and transpiration E_{ann} (lower row) during growing season per leaf area as a function of characteristic leaf length l_c for several combinations of the fraction of diffuse radiation k_d and atmospheric transmissivity τ. The leaf is oriented toward south and tilted against the horizontal by 45°. Atmospheric humidity and CO_2 are as given in Table 1.

which is understood to be incorporated into V_{max} and J_{max} as a factor. Phenological spring and autumn (i.e., daily mean temperatures are between 5°C and 10°C) occur during the time intervals $d_{i5} < d < d_{i10}$ and $d_{f10} < d < d_{f5}$, respectively (Figure 4a).

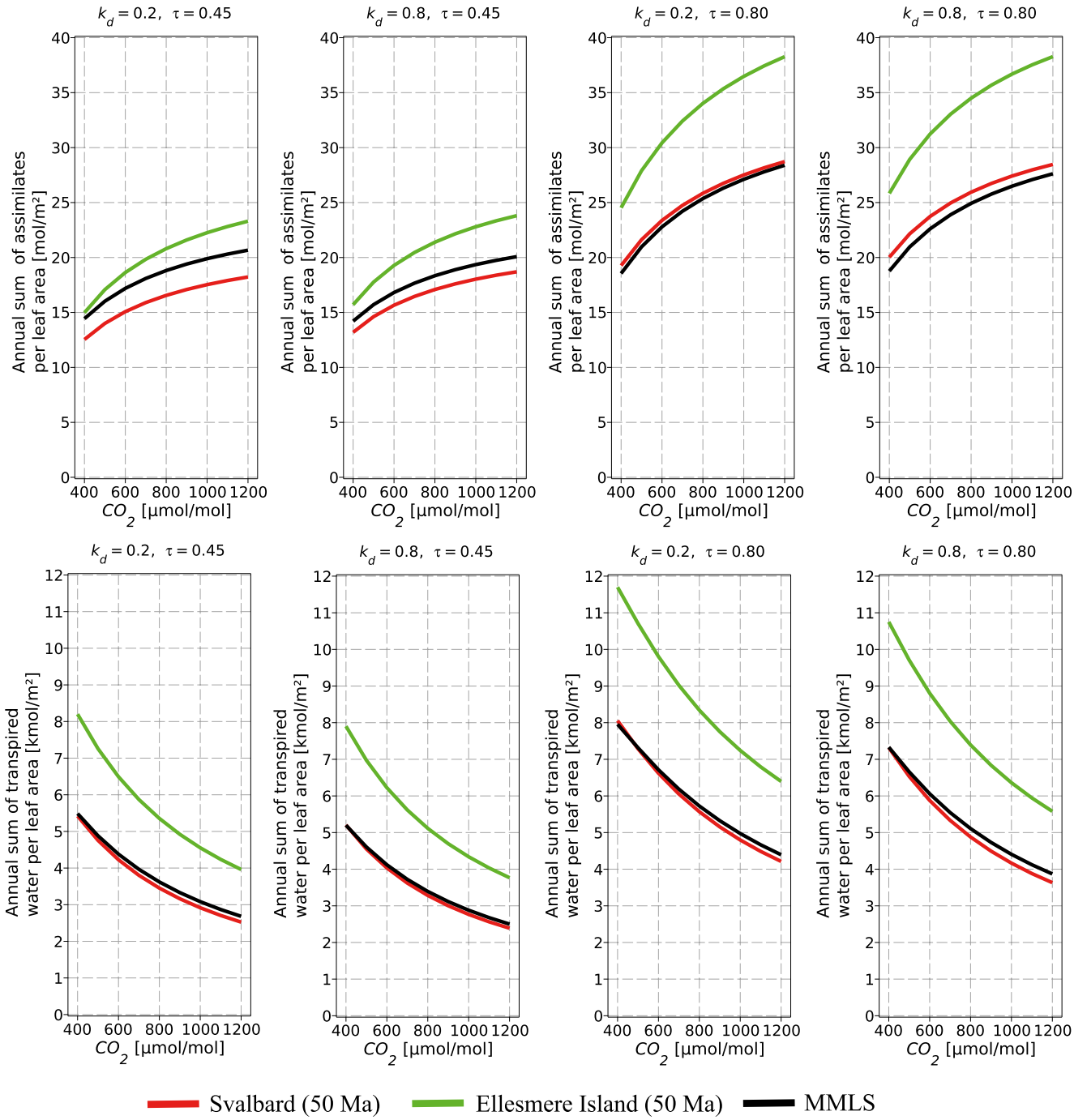

Figure 7. Annual assimilation A_{ann} (upper row) and transpiration E_{ann} (lower row) during growing season per leaf area as a function of atmospheric CO_2. Atmospheric humidity is as given in Table 1. The leaf is oriented toward south and tilted by 45° against the horizontal. Characteristic leaf length is l_c = 100 mm. Notice that the curve related to MMLS encompasses also $MMLS_{elevated}$.

3.6. Whole Tree Assimilation and Transpiration

Based on the model of gas exchange of single leaves, the primary productivity of an entire tree will be calculated. For this, a simple axisymmetric canopy model was derived for a tree whose crown is shaped as a cylinder of height h_c = 10 m and radius r_c = 4 m which is composed of 10 circular segments (see Figure 4). Each segment has a height of 1 m and a radius of 4 m and the midpoints of the segments are located along the axis of revolution (represented by the tree trunk).

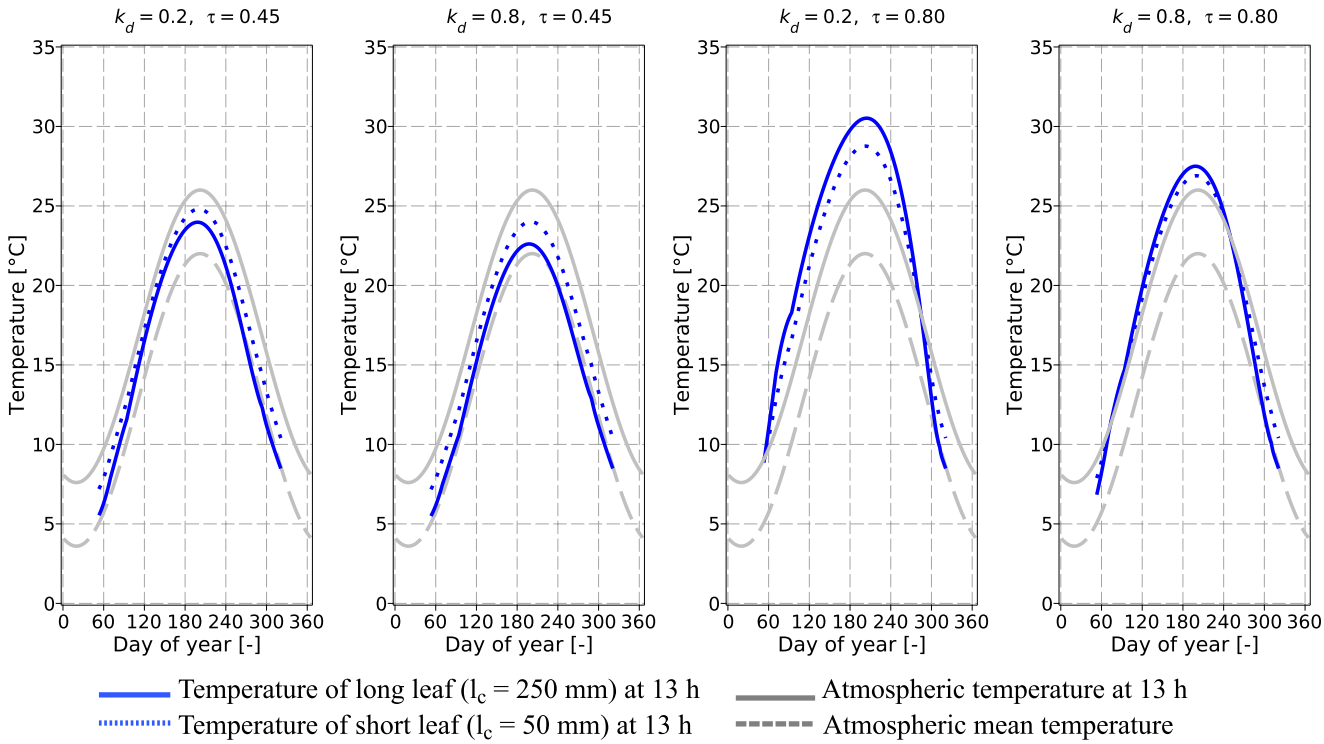

Figure 8. Variation of atmospheric mean temperature (dashed gray curve), atmospheric temperature at 13 hr (solid gray curve) and leaf temperatures at 13 hr of smaller leaves (l_c = 50 mm, dotted blue line) and larger leaves (l_c = 250 mm, solid blue line) as a function of day of year for a leaf that is oriented toward south and tilted by 45° against the horizontal at location Ellesmere Island.

For a tree canopy model, it is necessary to consider that assimilation and transpiration rates vary within the crown (Lalic et al., 2013; Lalic & Mihailovic, 2004; Vinod et al., 2022). This variation is caused by two factors: (a) leaves are not uniformly distributed within the crown, (b) the solar radiation becomes attenuated on its way through the crown because the leaves shade each other.

To quantify these effects we need submodels for leaf area density (LAD) and for the radiation profile within the crown. These are presented in Appendix D.

3.7. Calculation of Numeric Results

The figures, apart from Figures 1, 4 and A1, have been produced with the computer algebra system `maple` (Maplesoft, 2022). The results shown in Figures 6 and 7 were obtained using the following two approximations: (a) The

Table 3
Annual Sum Total of Transpiration (E_{tot}), Respiration ($R_{d,tot}$) and Assimilation (A_{tot}), for a Tree With a Cylindrical Crown of Height h_c = 10 m and Radius r_c = 4 m for Atmospheric Transmissivities τ = 0.45 and τ = 0.80 (Notice That for Horizontally Oriented Leaves the Difference Between Diffuse and Direct Light Becomes Meaningless, as Is Shown in Appendix B)

	Svalbard		Ellesmere Island		MMLS		$MMLS_{elevated}$	
τ	0.45	0.80	0.45	0.80	0.45	0.80	0.45	0.80
E_{tot} [kmol/a]	626.2	813.3	954.4	1,243.0	930.9	1,150.8	596.8	759.2
$R_{d,tot}$ [kmol/a]	3.7	3.8	5.0	5.2	3.8	4.0	3.8	4.0
A_{tot} [kmol/a]	3.0	4.8	3.6	6.4	2.6	3.5	3.3	4.4
$\bar{A}_{tot}$ [g C/m²/a]	716	1,146	859	1,528	621	836	788	1,050

Note. To facilitate comparison with measured values of net primary production (NPP), the bottom row shows the total assimilated annual carbon mass per ground area $\bar{A}_{tot}$. It is calculated from the A_{tot}-values of the third row according to $\bar{A}_{tot} = A_{tot}\, m_{mol} / (\pi r_c^2)$ where $m_{mol} \approx 12$ g/mol is the molar mass of carbon and $\pi r_c^2 = 50$ m² is the tree's ground area.

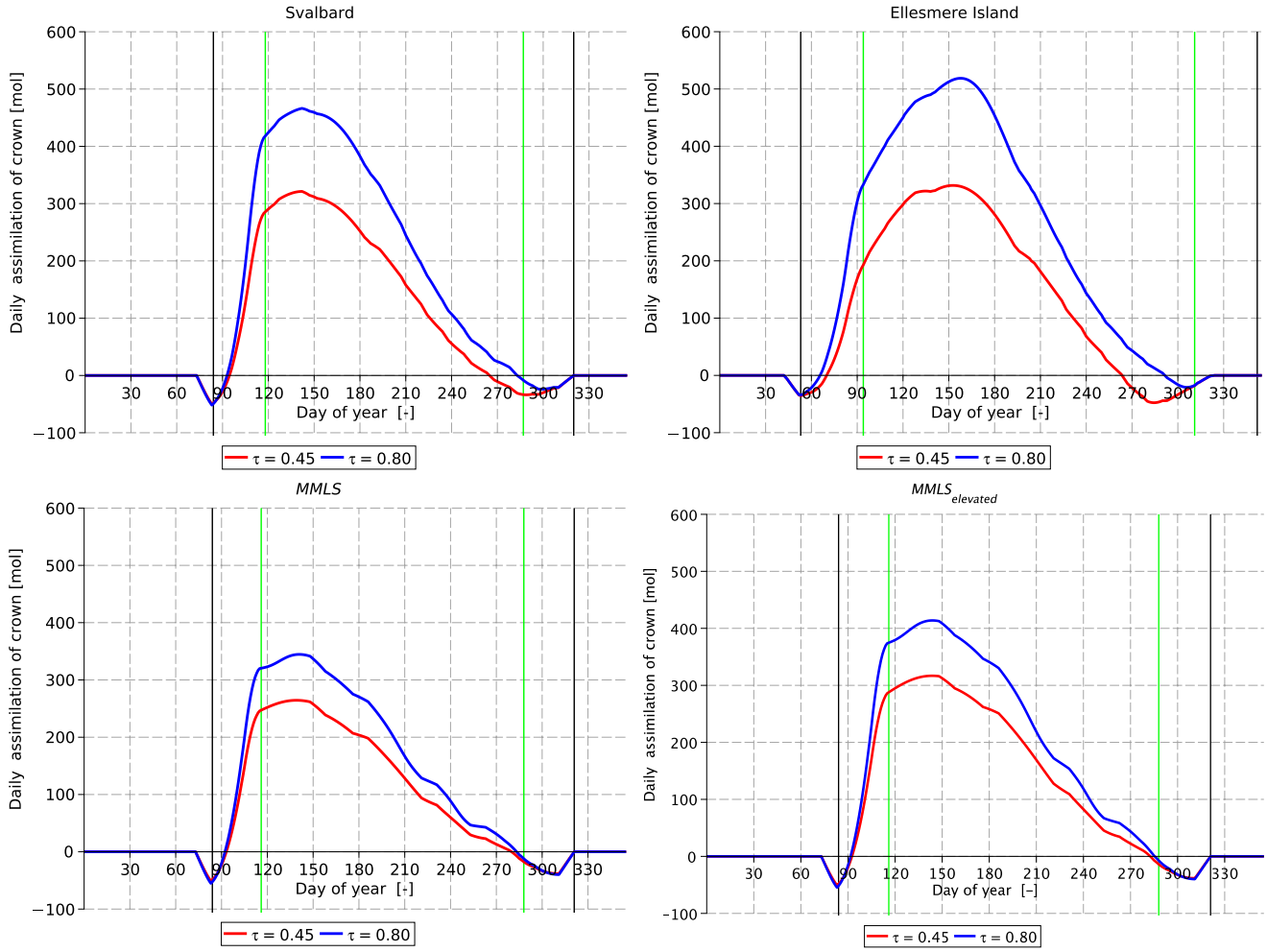

Figure 9. Whole tree assimilation A_d as a function of the day of the year (Equation D7). Red curves are related to $\tau = 0.45$, blue curves to $\tau = 0.80$. The leaves are horizontally oriented. Phenological spring and autumn season (defined by daily mean temperatures between 5° and 10°C) are indicated by pairs of vertical lines. At the beginning and the end of the growing season respiration is outpacing carbon uptake which leads to a negative carbon balance. Respiration of other plant parts (roots, stem, branches) which would occur in trees during winter is not included.

curves in Figure 6 are fitted curves through the calculated A_{ann}- and E_{ann}-values related to the characteristic leaf lengths $l_c = 1$, 50, 100, 150, 200, 250 and 300 mm. A similar procedure was applied to create Figure 7, based on the A_{ann}- and E_{ann}-results calculated for the CO_2 input values $C_a = 400$, 500, 600, 700, 800, 900, 1,000, 1,100 and 1,200 µmol/mol. (b) In order to keep computing time for the A_{ann}- and E_{ann}-values on a tolerable level, the daily sums of assimilation and transpiration were obtained by calculating A and E (i.e., assimilation and transpiration per leaf area and second) on the hour, multiplying by 3,600 s and then adding the results of the given day (see also the Data Availability Statement Section).

4. Results

4.1. Annual Cycles of Temperature, Length of Daylight and Irradiation

The annual variations of the daily mean temperatures of the three locations are shown in Figure 2a. For Svalbard and the MMLS they are almost identical and somewhat lower than for Ellesmere Island. With respect to annual distribution of daylight, both polar sites are almost identical and substantially different from the MMLS (Figure 2b).

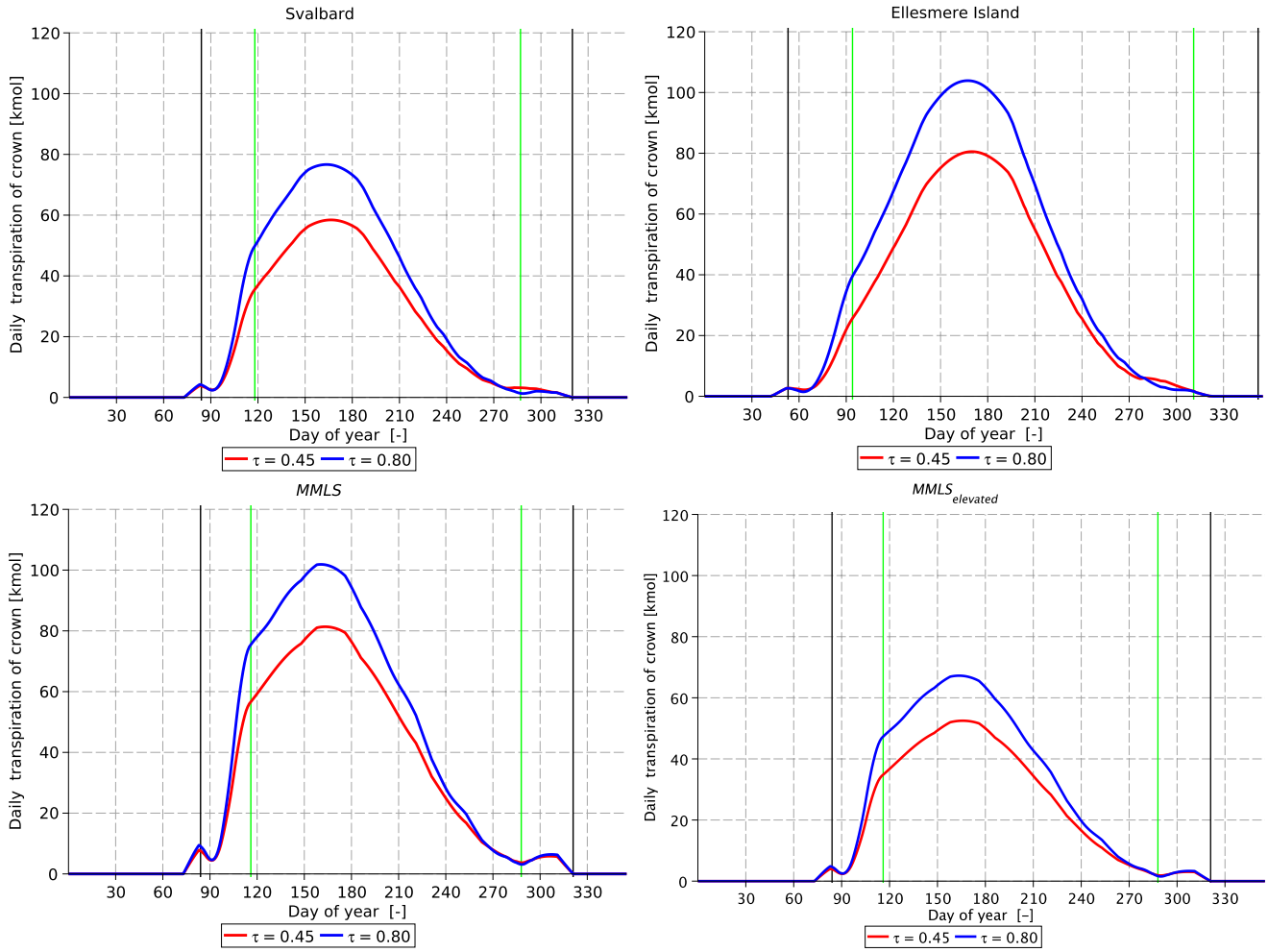

Figure 10. Whole tree transpiration E_d as a function of the day of the year. Red curves are related to $\tau = 0.45$, blue curves to $\tau = 0.80$. The leaves are horizontally oriented. Phenological spring and autumn season (defined by daily mean temperatures between 5° and 10°C) are indicated by pairs of vertical lines.

Figure 3 shows that the daily sum of irradiation during the growing season is highly affected by the atmospheric transmissivity τ and, to a much lower degree, by geographic latitude. Unsurprisingly, in view of the daylight distribution (Figure 2b), the irradiation received by the polar sites is almost identical.

Figure 5 shows the phenological phases as defined in Section 3.4 in relation to the annual distribution of daylight length. Interestingly, the small difference of palaeolatitude between Ellesmere Island (69.70°N) and Svalbard (67.94°N) causes a substantial difference in the number of polar nights (no sun hours) and polar days (24 sun hours) between these two sites (see Table 1): Ellesmere Island has about twice as much days per year with such extreme light conditions as Svalbard. Accordingly, the number of days with more moderate light conditions is higher at Svalbard than at Ellesmere Island.

The basic characteristics of the phenological seasons at the Eocene polar forests will be briefly described in the following.

4.1.1. Winter

The phenological winter season at Ellesmere Island lasts 65 days which is only as half as long as at Svalbard (128 days) and at the MMLS (127 days). As is to be expected from the site latitudes, the number of potential sun hours at MMLS (1,162 hr) is much higher than at the polar sites (Svalbard: 565 hr = 49% of MMLS, Ellesmere Island: 152 hr = 13% of MMLS).

4.1.2. Springtime

At Ellesmere Island the springtime season lasts 41 days which is 8 days longer than at Svalbard and at the MMLS. Svalbard, however, receives sunlight for 484 hr, roughly 40 hr more than the other two sites.

4.1.3. Summer

Summer is longest at Ellesmere Island (218 days) whereas Svalbard (170 days) and MMLS (173 days) attain only 78% and the 79% of this value, respectively. Due to the differences in daylight length between MMLS and the polar region, Ellesmere Island (3,751 hr) and Svalbard (3,117 hr) receive much more sunlight than the mid-latitude site MMLS (2,481 hr).

4.1.4. Autumn

Autumn lasts somewhat longer in Ellesmere Island (41 days) than in Svalbard (34 days) and the MMLS (32 days). These values are very similar to the duration of springtime at the three locations. In contrast, the numbers of potential sun hours during autumn are much smaller at springtime: the most sunshine is received by MMLS (303 hr), followed by Svalbard (217 hr = 72% of MMLS) and, far behind, Ellesmere Island (38 hr = 12% of MMLS).

At first sight, it may be confusing that MMLS has 1,162 hr sunshine during Winter, yet merely 484 hr in Spring. The reason for this is that the calculation of sun hours is not based on the astronomical definition of the seasons but on the phenological definition which employs daily mean temperatures ($T_a < 5$°C: Winter; $T_a > 10$°C: summer; 5°C $< T_a <$ 10°C: springtime or autumn, according to Section 3.4). Figure 5 is helpful in disentangling the puzzle: it shows that phenological Spring at MMLS lasts only 33 days, whereas phenological Winter (albeit with less sun hours per day) lasts 127 days. Similarly puzzling is the large difference between sun hours in the Autumn in contrast to Spring. This effect can be traced back to the "phase shift" between the maximum of daylight length—occurring at 21. June—and the temperature maximum which we assume to occur 1 month later (i.e., warmest day at 21. Juli). Thus, during the phenologically springtime which is defined via temperature the sun is already "higher above the horizon" than during phenological autumn and can produce more sun hours.

4.2. Gas Exchange

Figure 6 shows the annual sums of assimilation A_{ann} and transpiration E_{ann} per leaf area plotted against leaf size for different combinations of atmospheric transmissivity τ and the fraction k_d of diffuse irradiation. The environmental parameters are site-specific (see Figures 2 and 5 and Table 2). The leaf is oriented toward south and tilted against the horizontal by 45° (Sensitivity of assimilation against variation of cardinal direction and tilting angle of the leaf is calculated and discussed in Appendix F).

Highest A_{ann} is achieved by Ellesmere Island and lowest A_{ann} by the MMLS. For E_{ann}, MMLS and Ellesmere Island show the highest values and Svalbard the lowest. High transmissivity enhances both A_{ann} and E_{ann}, regardless of diffusivity which can, however, modulate gas exchange responses somewhat. Overall, however, the influence of k_d is low.

The effect of leaf size on gas exchange is complex. Under favorable conditions, meaning high transmissivity (and therefore high irradiation) and low diffusivity, A_{ann} increases for all locations, as does E_{ann}. For high irradiation with a high amount of diffuse light A_{ann} and E_{ann} increase with leaf size for Svalbard, MMLS and $\text{MMLS}_{\text{elevated}}$. For Ellesmere Island, both A_{ann} and E_{ann} decrease with leaf size under these conditions. For low transmissivity, however, A_{ann} as well as E_{ann} decrease with leaf size for all sites, regardless of diffusivity.

An increase of transpiration with leaf size under high transmissivity and low diffusivity is to be expected and supports the idea that smaller leaves can save water under these conditions. A decline of both A_{ann} and E_{ann} with leaf size, as happens particularly under low transmissivity, is, however, counterintuitive and will be considered in more detail in the discussion section.

The effect of CO_2 on gas exchange is indicated in Figure 6 by the results for $\text{MMLS}_{\text{elevated}}$ which are similar to those of Svalbard. Figure 7, showing A_{ann} and E_{ann} against CO_2, further illustrates the influence of CO_2 on gas exchange under different combinations of transmissivity and diffusivity for a leaf with a fixed leaf size and tilted against the horizontal by 45°. A_{ann} increases with CO_2 for all cases whereas E_{ann} declines with CO_2. Note that the

gas exchange results for MMLS and Svalbard are identical or almost identical in Figure 7, with the exception of A_{ann} under low transmissivity. Here, MMLS achieves higher values.

4.3. Leaf Temperature and Leaf Size

Figure 8 shows for Ellesmere Island the annual course of leaf temperature for a smaller leaf ($l_c = 50$ mm), a larger leaf ($l_c = 250$ mm) and air temperature at noon (i.e., 13 hr), together with the annual course of mean air temperature. Also here, different combinations of transmissivity and diffusivity were selected: lower and higher transmissivity combined with lower and higher diffusivity. For high transmissivity and low diffusivity (meaning a high fraction of direct light), during spring and summer, leaf temperatures can be up to about 5°C higher than air temperature, particularly for larger leaves. Under low transmissivity, leaf temperature is somewhat lower than air temperature, especially for large leaves. Additional variations of leaf orientation and leaf inclination resulted in leaf temperatures which are in the range of the results shown in Figure 8. These additional variations are summarized in Appendix F.

4.4. Whole Tree Assimilation and Transpiration

Until now, assimilation and transpiration rates were calculated for a single leaf at the periphery of the tree crown, thereby fully exposed to irradiation. In the following, gas exchange will be derived for a whole tree, based on the approach described in Section 3.6. Table 3 summarizes the main results of annual assimilation and transpiration of a tree. Figures 9 and 10 show daily rates of tree assimilation and transpiration throughout a year for the two Arctic sites and for the MMLS and $\text{MMLS}_{\text{elevated}}$.

The annual course of gas exchange shows a strong increase early in spring, followed by a gradual decrease during summer and autumn, reflecting the development of leaf senescence (Figure 4a). Tree productivity increases with atmospheric transmissivity, as expected, and is highest for Ellesmere Island and lowest for MMLS (Table 3, Figure 9). Transpiration rates are also highest at Ellesmere (Table 3, Figure 10). The lowest values for A_{ann} result for the MMLS under lower transmissivity. For $\text{MMLS}_{\text{elevated}}$, tree productivity becomes similar to that of Svalbard.

5. Discussion

5.1. Gas Exchange Under Arctic Eocene Conditions and the Role of CO_2

An essential result of this study is that conditions of the Eocene Arctic potentially enhanced photosynthesis and therefore tree primary productivity to such an extent that assimilation rates at high-latitude sites are up to 30%–60% higher as for a modern temperate mid-latitude site (MMLS). CO_2 is among the main factors for this enhancement as is illustrated by the effect of elevated CO_2 on gas exchange (Figures 6 and 7): both photosynthesis and transpiration of the $\text{MMLS}_{\text{elevated}}$ are similar to the results of Svalbard. Whereas assimilation is promoted by elevated CO_2 at the Eocene Arctic sites, transpiration rates are reduced. This is illustrated by the results of the $\text{MMLS}_{\text{elevated}}$ (Figure 6) and the CO_2 variation runs (Figure 7). Reduced transpiration and ample precipitation, according to available palaeoclimate data (Huber & Goldner, 2012; West et al., 2015, 2020), indicate that water was apparently not a limiting resource at the Eocene polar sites.

A_{ann} of $\text{MMLS}_{\text{elevated}}$ is, however, still lower compared to that of Ellesmere Island (Figure 6). This indicates additional factors which can further promote assimilation at Eocene Arctic sites. These are temperature and the day length of the growing season which are both highest for Ellesmere Island. Leaf temperature enhances assimilation until an optimum is reached (Bernacchi et al., 2003; Konrad et al., 2020). Accordingly, Ellesmere Island shows the highest MAT. As illustrated by Figures 2 and 5, Ellesmere also receives the highest amount of daylight hours because the annual period of 24 hr day light length during the summer is longest for this site. Photosynthesis is especially promoted by a high day length during early summer, because photosynthetic capacity of deciduous taxa peaks exactly during that time (Figure 4a).

5.2. Productivity of the Early Eocene Arctic Canopy

Enhanced leaf photosynthesis is expected to lead to higher primary productivity of a tree. As indicated by the results of the canopy model listed in Table 3 and shown in Figure 9, primary productivity of the Eocene sites

was about 30%–60% higher than that of the MMLS, thereby reaching productivity levels of extant tropical forests (Cleveland et al., 2011; Turner et al., 2006; Zhao et al., 2005). How realistic are these results? The ability of the canopy model to provide reliable data from single-leaf values can be evaluated by comparing the results for the MMLS with extant primary productivity data provided by the MODIS NPP data set for the immediate surroundings of this location (Neumann et al., 2016).

To achieve this, only those grid cells of NPP were selected which (a) are covered by broad-leaved forests according to the Corine Land Cover Data 2018 (https://land.copernicus.eu/pan-european/corine-land-cover/clc2018) and (b) are within the $0.5° \times 0.5°$ global grid cell which represents the MMLS (see Appendix G). The mean of these NPP-values constitutes a representative estimation of the NPP of the MMLS. The MODIS NPP data for the MMLS region—when limited to areas covered by deciduous forest—show an averaged primary productivity of 608 g C/m^2/a. The canopy model predicts (Table 3) 621 g C/m^2/a (for overcast sky, atmospheric transmissivity $\tau = 0.45$) to 836 g C/m^2/a (for clear sky, $\tau = 0.80$). Transmissivity data for Central Europe in fact indicate an overall average transmissivity close to 0.45 (Frank et al., 2018). The model therefore somewhat overestimates primary productivity, but can nonetheless be considered as providing satisfactorily realistic data. In addition, the productivity of the MMLS can be considered representative for temperate decidous hardwood forest (Turner et al., 2006; Zhao et al., 2005).

Another question is the possible impact of CO_2 on crown density and tree ecophysiology which may compromise the reliability of input parameters for the model approach. Available data from long-term experiments in which adult trees were exposed to elevated CO_2 indicate no or negligible influence of CO_2 on leaf density and LAI (Bader et al., 2013; Norby et al., 2022). Stimulation of photosynthesis by elevated CO_2 is usually indicated by results of gas exchange models and also found in experiments (Ainsworth & Long, 2005). Results of a long-term experiment with adult trees in an established forest also indicate the persistence of stimulated photosynthesis by elevated CO_2 (Bader et al., 2010). In another long-term experiment, however, a substantial decrease in photosynthesis was found, probably due to a lower soil nutrient availability (Norby et al., 2022). Limitation of available nutrients is therefore crucial for the enhancement of primary productivity by CO_2, information which is not normally available for fossil sites. Sufficient nutrient availability for the two polar sites may, however, be assumed because of the occurrence of large leaves which—besides correlating with high humidity—tend to be promoted by fertile soil conditions (Cunningham et al., 1999; Dolph & Dilcher, 1980; McDonald et al., 2003; Wright et al., 2017).

It has to be emphasized, however, that CO_2 stimulation of photosynthesis does not mean an automatic increase in growth and biomass accumulation rate. As already mentioned, LAI and leaf density of adult trees growing under conditions of a closed canopy were not found to be higher under elevated CO_2, despite stimulation of photosynthesis (Bader et al., 2010, 2013; Norby et al., 2022). Therefore, elevated CO_2 did not enhance leaf biomass production. Also, no increase in the accumulation rate of stem biomass was found (Bader et al., 2010, 2013; Norby et al., 2022). The lack of a detectable effect of higher photosynthesis on growth rate in adult trees forming a closed canopy is caused by the limitation of other resources than CO_2, particularly soil nutrients, but also space limitations (Körner, 2006). Photosynthesis stimulation then results in surplus assimilates which are exudated by the roots and promote growth of mycorrhiza and soil microbes (Prescott et al., 2020). It is, however, difficult to directly infer the ecophysiological behavior of fossil plants from observations made on extant plants. The production of surplus assimilates by extant trees under elevated CO_2 conditions, for instance, poses the question of whether photosynthesis parameters might have been downregulated in fossil plants, thereby reducing assimilation rate and surplus assimilates. This could also affect the demand for nutrients: less N may be required by leaves due to a decrease in Rubisco content (Dong et al., 2022). It should also be mentioned that Royer et al. (2005) found a decline in photosynthesis during a 24 hr light phase in potted saplings of various tree species which were cultivated under Eocene high latitude conditions (light, temperature and CO_2). With these caveats in mind, the results of this study indicate a potential for primary productivity of the Eocene fossil sites which is similar to modern tropical sites.

5.3. Leaf Size, Diffuse Radiation and Atmospheric Transmissivity

The occurrence of large deciduous leaves in fossil material from high latitudes was noted since the first comprehensive descriptions of polar fossil floras by Heer (1859). Principally, leaf size is positively correlated with

growing season temperature, humidity and availability of nutrients, meaning that large leaves occur preferentially under favorable conditions (Cunningham et al., 1999; Dolph & Dilcher, 1980; McDonald et al., 2003; Wright et al., 2017). Leaf size is therefore used as a palaeo-precipitation proxy (Royer et al., 2005; Wilf et al., 1998). In fact, large leaves from various broad-leaved taxa contribute to the CLAMP signal of high precipitation rates for the Arctic early Eocene, which is also consistent with climate modeling (West et al., 2015).

Large leaf size in fossil material from Arctic angiosperms is, however, also ascribed to special light conditions of the high latitudes. Wolfe (1985) explained the large leaf size of Arctic fossil taxa as a response to the low angle of incidence of solar radiation. This low angle would prevent leaf overheating, making, first, large leaves possible and, second, would promote photosynthesis by providing a larger assimilating area. Also West et al. (2015, 2020) discuss large fossil leaves at polar high latitudes as being caused by light: high proportions of diffuse light would lead to large leaves, similar to extant shade leaves. A light-induced positive effect on leaf size would possibly cause a bias in leaf-based palaeoprecipitation proxies by overestimating precipitation rates (West et al., 2020).

The incidence of solar radiation was included in the model, and the results indicate no beneficial effects of leaf size under high latitude conditions of light incidence. Also, no clear benefit of leaf size in case of a high fraction of diffuse irradiation could be detected. With a high diffusivity, both A_{ann} and E_{ann} mostly decrease with leaf size (Figure 6). The effect of atmospheric transmissivity τ on assimilation, however, is considerably higher than that of diffusivity k_d (Figure 6). In fact, the results are as to be expected: a high transmissivity allows for high assimilation and transpiration rates, particularly when accompanied by a low diffusivity (meaning a clear sky and high irradiation) whereas low values of transmissivity (meaning an overcast sky with low irradiation) leads to low assimilation and transpiration rates. Under these conditions, A_{ann} as well as E_{ann} decline with leaf size, regardless of the diffusivity conditions (Figure 6). A decline in E_{ann} with leaf size, however, appears to be counterintuitive, because larger leaves are expected to heat up stronger than smaller leaves and, therefore, higher transpiration is expected for larger leaves.

The question arises why E_{ann} and A_{ann} decline with increasing leaf size. The negative effect of leaf size on gas exchange, as resulting particularly for low transmissivity, can be traced back to Equation 2 which balances the energy exchange of the leaf and depends on characteristic leaf length l_c. The left hand side of this equation quantifies the radiative energy flux into the leaf emanating from various sources (sun, sky and surroundings). The three terms on the right hand side are more diverse: the first one quantifies infrared radiation (IR) emitted by the leaf, the second one heat exchange via the air by conduction and convection and the third one evaporative cooling by transpiration. The radiative and the evaporative terms are always positive whereas the conduction/convection term can change sign, meaning that heat can be either transported off the leaf (leaf cooling), when the air is cooler than the leaf, or into the leaf, when the air is warmer than the leaf (leaf heating).

Leaf size is introduced into these processes via its influence on leaf boundary layer thickness d_{bl} (Equation 3) and leaf boundary layer conductance K_a/d_{bl} which appears on the right hand side of Equation 2. Note that all three flux terms on the right hand side of Equation 2 depend (at least implicitly) on l_c. Note also that the left hand side of Equation 2—the energy input by radiation—is independent of l_c. It is important to realize that—according to Equation 2—the conduction/convection flux decreases with increasing l_c, that is, its fraction of the flux balance is higher for smaller leaves than for larger leaves. In Appendix E, exemplary calculations for the various items of this energy budget are illustrated for the location Svalbard. One example, depicted in Figure E2 and showing the various components of the leaf energy budget, illustrates how a decline in transpiration with increasing leaf size can happen. As visible in Figure E2, air temperature is low under low transmissivity during a summer day, as well as radiative energy input into the leaf. The leaf, however, emits IR depressing leaf temperature below air temperature. Under these conditions, transpiration is low. There is, however, energy input into the leaf from the air by conduction and convection (the air "tries" to heat up the leaf). This energy input declines with leaf size because of the growing boundary layer thickness. Therefore, smaller leaves will become warmer than larger leaves. Warming means, however, increased transpiration. To put it briefly: under these conditions, warming by conduction and convection promotes transpiration in smaller leaves. Since warming also promotes photosynthesis, both processes are under these circumstances higher in smaller leaves compared to larger leaves. There are more detailed examples and explanations in Appendix E.

The coupling between gas and heat exchange makes the association between leaf size, leaf temperature and latent heat complex, and counterintuitive effects can occur, depending on the environmental situation. It should also be emphasized that the results shown in Figures 6 and 7 are based on the annual sums A_{ann} and E_{ann} of these processes, adding more complexity to these relationships. At any rate, no convincing benefits from large leaf

size as specific for the polar sites could be identified. A reduction in transpiration, as found for larger leaves under low transmissivity, might be considered advantageous. Assimilation is, however, also reduced under these conditions and there is no evidence for water shortage for the Eocene polar sites, as already discussed. As was noted by Wright et al. (2017), large leaves appear to be favored whenever possible. The reasons are, however, not completely understood.

6. Conclusions

1. Photosynthesis is enhanced under conditions of the Arctic Eocene, particularly by elevated CO_2. Higher site-specific growing season temperatures and 24 hr daylight length further promote photosynthesis, leading to highest annual photosynthesis at Ellesmere Island.
2. The influence of leaf size on gas exchange is complex. No specific selective advantage for large leaf size under Arctic Eocene conditions could be detected.
3. The results of this study indicate a potential for substantially higher productivity of high latitude forests of the Eocene compared to extant temperate deciduous forests. The potential productivity found for Ellesmere Island is in the range of modern tropical forests. Whether this potential was realized or not depends on nutrient availability and possible evolutionary changes in leaf function.

Appendix A: Celestial Mechanics

To describe the sun's position we use a (local) horizontal coordinate system as depicted in Figure A1; ϑ denotes the altitude of the sun above the horizon, η its azimuth. ϑ varies according to

$$\vartheta = \arcsin(\sin\delta \sin\lambda - \cos\delta \cos\lambda \cos\eta) \tag{A1}$$

where $\eta = \omega t$ with $\omega = 2\pi/(24\text{ hr}) = 2\pi/(24 \times 60 \times 60\text{ s})$ and t is time of day. (The minus sign is due to the fact that we relate η to the Northern direction.) The altitude ϑ depends also on geographical latitude λ and on the current declination

$$\delta = -23.5° \cos\left(\frac{2\pi(d+10)}{365.25}\right) \tag{A2}$$

where d denotes the day of the year.

In a coordinate system that is centered at the leaf (see Figure A1) with x-, y- and z-axis pointing to the North, to the East and to the Zenith, respectively, the unit vector pointing from the leaf to the sun can be written

$$\mathbf{n_b} = \cos\eta \cos\vartheta\, \mathbf{e_x} + \sin\eta \cos\vartheta\, \mathbf{e_y} + \sin\vartheta\, \mathbf{e_z} \tag{A3}$$

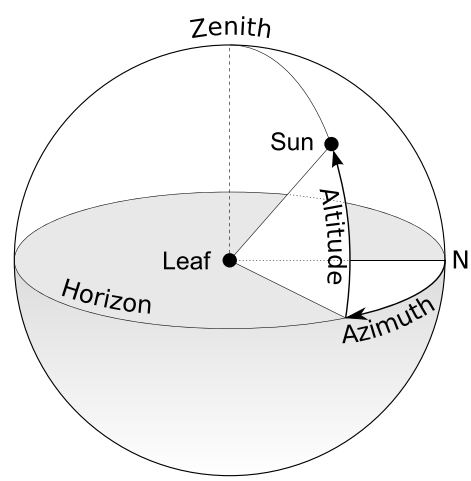

Figure A1. Horizontal coordinate system.

where $\mathbf{e_x}$, $\mathbf{e_y}$ and $\mathbf{e_z}$ denote the unit vectors into the x-, y-, and z-direction, respectively, and η and ϑ denote azimuth and altitude of the sun, respectively.

We describe the orientation of a (flat) leaf by the direction of the unit vector $\mathbf{n_l}$ (oriented normal to the leaf plane)

$$\mathbf{n_l} = \cos H \cos\Theta\, \mathbf{e_x} + \sin H \cos\Theta\, \mathbf{e_y} + \sin\Theta\, \mathbf{e_z} \tag{A4}$$

where H and Θ denote azimuth and altitude angle, respectively, of the vector $\mathbf{n_l}$.

For a solar radiation beam with irradiance I_n directed along $\mathbf{n_b}$ toward a leaf whose surface is *not* normal to the beam (i.e., $\mathbf{n_l} \neq \mathbf{n_b}$), the irradiance amounts to

$$I_l = I_n \cos\psi \tag{A5}$$

where ψ is the angle between $\mathbf{n_l}$ and $\mathbf{n_b}$. Using the relation $\cos\psi = \mathbf{n_l} \cdot \mathbf{n_b}$, Expressions A3 and A4 plus the identity

$$\sin x \sin y + \cos x \cos y = \cos(x - y) \tag{A6}$$

the angle ψ can be expressed as

$$\psi = \arccos[\cos\vartheta \cos\Theta \cos(\eta - H) + \sin\vartheta \sin\Theta] \tag{A7}$$

where ϑ, the altitude of the sun, is given by Expression A1.

Appendix B: Direct and Diffuse Irradiance, Attenuation of Direct Beam Irradiance

Total solar irradiance I_l on a leaf surface that is tilted with respect to the beam of (direct) radiation I_n by the angle ψ is given, according to Equation A5, by $I_l = I_n \cos\psi$. It can be divided into the beam component $I_{l,b}$ from direct irradiation and the diffuse component $I_{l,d}$

$$I_l = I_{l,b} + I_{l,d} \tag{B1}$$

Introducing the quantity k_d, the diffuse fraction of I_l, and using Equation A5, the direct (i.e., the non-diffuse) irradiation component of I_l can be written

$$I_{l,b} = (1 - k_d) I_l = (1 - k_d) \cos\psi\, I_n \tag{B2}$$

The diffuse irradiance component $I_{l,d}$, however, requires a model. To keep things simple we adopt in what follows an isotropic sky model which assumes that diffuse radiation is uniformly distributed over the sky dome and reflection on the ground is also diffuse. This assumption of isotropy allows to express the diffuse term in Equation B1 in the form (Liu & Jordan, 1960; Loutzenhiser et al., 2007)

$$I_{l,d} = I_h\, k_d \left(\frac{1 + \sin\Theta}{2}\right) + I_h\, \rho \left(\frac{1 - \sin\Theta}{2}\right) \tag{B3}$$

where ρ denotes the ground reflectance, Θ is—as defined in Equation A4—the altitude angle of the vector $\mathbf{n_l}$ that is normal to the leaf surface and

$$I_h = \sin\vartheta\, I_n \tag{B4}$$

is the global solar irradiance striking a horizontal leaf. Using Equations B2, B3 and B4 in Equation B1, the total solar irradiance on a tilted leaf can now be written as

$$I_l = I_n \left[\cos\psi\,(1 - k_d) + \sin\vartheta\, k_d \left(\frac{1 + \sin\Theta}{2}\right) + \sin\vartheta\, \rho \left(\frac{1 - \sin\Theta}{2}\right)\right] \tag{B5}$$

The quantity I_n in Equation B5 can be obtained by the following consideration: On its way through the atmosphere, direct radiation is attenuated by molecular scattering and absorption (with a negligible contribution from aerosol, see Monteith and Unsworth (2013); Nobel (2005)). Direct beam irradiance at sea level amounts to approximately

$$I_n = S_c \tau^{1/\sin\vartheta} \tag{B6}$$

where S_c is the solar constant, τ is the atmospheric transmissivity, and ϑ is the altitude of the sun above the horizon. A typical τ range on cloudless days is 0.45…0.8. Using Equation B6, Expression B5 for the incident radiation becomes

$$I_l = S_c \tau^{1/\sin\vartheta}\left[\cos\psi(1-k_d) + \sin\vartheta\, k_d\left(\frac{1+\sin\Theta}{2}\right) + \sin\vartheta\,\rho\left(\frac{1-\sin\Theta}{2}\right)\right] \tag{B7}$$

The slightly involved dependencies in Equation B7 imply that—apart from the atmospheric transmissivity τ, the altitude of the sun above the horizon ϑ, and the diffuse irradiance fraction k_d—the variables day of the year d, time of day t, geographical latitude λ, and the orientation of the leaf (in terms of its azimuth angle H and its altitude angle Θ) must be given as input values.

For horizontally oriented leaves (i.e., $\Theta = \pi/2$) Equations A7, B2, B3 and B7 simplify considerably to $\psi = \arccos(\sin\vartheta)$, $I_{l,b} = (1-k_d)\sin\vartheta\, I_n$, $I_{l,d} = k_d \sin\vartheta\, I_n$ and $I_l = S_c\tau^{1/\sin\ \vartheta}\sin\vartheta$, respectively. Notice, that the dependence of I_l on k_d disappears in this case, in agreement with the physics of the situation.

Appendix C: Model of Photosynthesis

We use the Farquhar model of assimilation (see Farquhar et al., 1980, 2001) for C_3-plants which gives the assimilation rate A in terms of C_i (the carbon dioxide concentration inside the leaf), the irradiance I_l, and various other variables:

$$A = \left(1 - \frac{\Gamma}{C_i}\right)\min\{W_c, W_j\} - R_d \tag{C1}$$

with

$$W_c := V_{max}\frac{C_i}{C_i + K_c\left(1+\frac{p_o}{K_o}\right)}$$
$$W_j := \left(\frac{2}{9}J\right)\frac{C_i}{C_i + \frac{7}{3}\Gamma}$$

where

$$J := \frac{Q_2 + J_{max} - \sqrt{(Q_2 + J_{max})^2 - 4\,\Theta_{PSII}\,Q_2\,J_{max}}}{2\Theta_{PSII}}$$

and

$$Q_2 := Q\alpha_l\Phi_{PSII,max}\,\beta \tag{C2}$$

The expression $\min\{W_c, W_j\}$ denotes the smaller of W_c and W_j for given values of C_i and J. The variables and parameters used in Equation C1 are defined in Table 2. Defining

$$q = \begin{cases} V_{max} & \text{if } W_c < W_j \\ \frac{2}{9}J & \text{if } W_c > W_j \end{cases} \tag{C3}$$

and

$$K = \begin{cases} K_c\left(1+\frac{p_o}{K_o}\right) & \text{if } W_c < W_j \\ \frac{7}{3}\Gamma & \text{if } W_c > W_j \end{cases} \tag{C4}$$

Expression C1 can be written in the more compact form

$$A = q\,\frac{C_i - \Gamma}{C_i + K} - R_d \tag{C5}$$

Most of the variables defining photosynthesis depend on the leaf temperature T_l (measured in Kelvin). In order to quantify their temperature dependance we use the parametrizations given by Bernacchi et al. (2003):

$$\begin{aligned}
J_{max} &= J_{max,25^\circ\mathrm{C}} \times \mathrm{e}^{\left(17.57 - \frac{5236.760760}{T_l}\right)} \times \mu\mathrm{mol/m^2/s}\\
K_c &= \mathrm{e}^{\left(38.05 - \frac{9553.420009}{T_l}\right)} \times \mu\mathrm{mol/mol}\\
K_o &= \mathrm{e}^{\left(20.30 - \frac{4375.593855}{T_l}\right)} \times \mathrm{mmol/mol}\\
p_o &= 210\,\mathrm{mmol/mol}\\
R_d &= R_{d,25^\circ\mathrm{C}} \times \mathrm{e}^{\left(18.72 - \frac{5579.543675}{T_l}\right)} \times \mu\mathrm{mol/m^2/s}\\
V_{max} &= V_{max,25^\circ\mathrm{C}} \times \mathrm{e}^{\left(26.35 - \frac{7857.546634}{T_l}\right)} \times \mu\mathrm{mol/m^2/s}\\
\Gamma &= \mathrm{e}^{\left(19.02 - \frac{4549.992181}{T_l}\right)} \times \mu\mathrm{mol/mol}\\
\Theta_{PSII} &= -31.76 + 0.22\,T_l - 0.00037\,T_l^2\\
\Phi_{PSII,max} &= -31.025 + 0.20\,T_l - 0.00034\,T_l^2
\end{aligned} \tag{C6}$$

T_l is measured in Kelvin. The factors $V_{max,25^\circ\mathrm{C}}$, $R_{d,25^\circ\mathrm{C}}$ and $J_{max,25^\circ\mathrm{C}}$ which are part of the expressions V_{max}, R_d and J_{max} must be known (or calibrated).

Solar irradiation I_l (see section Appendix B) is given in terms of energy per area per time (usually in units J/m^2/s), photosynthesis processes, however, utilize only the photosynthetically active fraction Q of the incoming radiation (see section Appendix C), given in terms of number of photosynthetically active photons per area per time (usually in units mol/m^2/s).

To convert the former to the latter, we define the conversion factor ζ via

$$Q = \zeta\, I_l \tag{C7}$$

and assign it the popular (Larcher, 2003) value $\zeta = 5 \times 10^{-6}$ mol/J.

Appendix D: Models for Leaf Area Density and Radiation Profile Within the Crown

D1. Leaf Area Density

For the leaf area density (LAD) we use the model of Lalic et al. (2013) which assumes, for simplicity, that leaf number density varies within the crown primarily vertically, and that the horizontal variation is negligible, in comparison. Examination of real trees suggests to model LAD by the expression (Figure 4b)

$$\mathrm{LAD}(z) = L_m \left[\frac{h_c - z_m}{h_c - z}\right]^n \exp\left(n\left[1 - \frac{h_c - z_m}{h_c - z}\right]\right) \tag{D1}$$

where

$$n = \begin{cases} 6 & 0 < z < z_m \\ 1/2 & z_m < z < h_c \end{cases} \tag{D2}$$

z denotes the vertical coordinate, L_m is the maximum value of LAD and z_m is the corresponding height, defined by the relation $\mathrm{LAD}(z_m) = L_m$. Leaf area index (LAI) follows from LAD via the integral $\mathrm{LAI} = \int_0^{h_c} \mathrm{LAD}(z)\,dz$ (Figure D1).

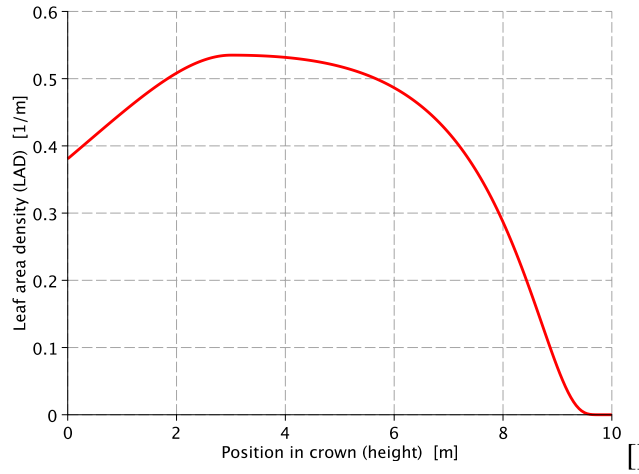

Figure D1. Leaf area density (LAD) as a function of vertical position z in the tree, as given by Equation D1 ($z = 0$ and $z = h_c$ represent bottom respective top of the crown).

D2. Radiation Profile Within the Crown

The radiation profile within the crown can be described by an attenuation factor that is derived from the Lambert-Beer law (Lalic et al., 2013) and from the leaf area density. Inclusion of the attenuation factor leads to the following redefinition of Equation C7 of section Appendix C:

$$Q(z) = \zeta I_l \exp\left[-\frac{k}{\cos\vartheta}\int_{h_c}^{z} \mathrm{LAD}(z)\, dz\right] \tag{D3}$$

with the extinction coefficient k and the altitude angle ϑ (see section Appendix A). That means, Q, the number of photosynthetically active photons per area and time (see section Appendix C), depends no longer only on I_l, the total solar irradiance defined in Equation B1 of section Appendix B, but also on the position of the assimilating site within the crown and the extinction capacity of the crown for a given light ray.

D3. Whole Tree Assimilation

Expressions D1 and D3 allow to calculate assimilation and transpiration rates of a whole tree—in contrast to the hitherto developed approach for single leaves on the outer margin of the tree crown.

To start, we define the assimilation rate per volume,

$$A_v = \mathrm{LAD}(z)\, A \tag{D4}$$

that is, the product of the leaf area density LAD(z) (see Equation D1) and the leaf-based assimilation rate A (defined in terms of photosynthetic parameters in Equation C1). The mutual shading effect is included in A by Equation D3, as described in section Appendix D. The daily and annual sums of assimilation per volume at a given crown position z is then obtained by integrating A_v for all $d = 1\ldots365$ with respect to time

$$A_{d,v} = \int_{t=0}^{24\,\mathrm{h}} A_v\, dt = \int_{t=0}^{24\,\mathrm{h}} \mathrm{LAD}(z)\, A\, dt \tag{D5}$$

and by adding all $A_{d,v}$, resulting in

$$A_{a,v} = \sum_{d=1}^{365} A_{d,v} = \sum_{d=1}^{365} \int_{t=0}^{24\,\mathrm{h}} \mathrm{LAD}(z)\, A\, dt \tag{D6}$$

The whole tree value of assimilation as a function of the day of the year d is obtained by a spatial integration of $A_{d,v}$ over the volume of the tree crown,

$$A_d = \pi r_c^2 \int_{z=0}^{h_c} A_{d,v}\, dz = \pi r_c^2 \int_{z=0}^{h_c} \int_{t=0}^{24\,\mathrm{h}} \mathrm{LAD}(z)\, A\, dt\, dz \tag{D7}$$

where r_c and h_c denote radius and height of the tree crown. Finally, the whole tree value of assimilation for a whole season is obtained by adding the daily values A_d of Equation D7 over the whole year:

$$A_{tot} = \sum_{d=1}^{365} A_d = \pi r_c^2 \sum_{d=1}^{365} \int_{z=0}^{h_c} \int_{t=0}^{24\,\mathrm{h}} \mathrm{LAD}(z)\, A\, dt\, dz \tag{D8}$$

Similar expressions apply for transpiration rates etc.

Appendix E: Energy Exchange Between Leaf and Environment

As noted above (and ilustrated by Figure 6), atmospheric transmissivity τ determines if assimilation and transpiration increase or decrease with leaf size. This interdependence can be traced back to the leaf energy balance Equation 2.

$$aI_l + a_{IR}\,\sigma\left(T_{surr}^4 + T_{sky}^4\right) \approx 2e_{IR}\,\sigma T_l^4 + \frac{2K_a}{d_{bl}}(T_l - T_a) + 2H_{vap}\,[w_l(T_l) - w_a]\bar{a}\,g(T_l) \tag{E1}$$

The left hand side of this equarion consists only of radiative energy fluxes into the leaf. The three terms on the right hand side are more diverse: the first one quantifies radiation emitted by the leaf, the second one heat exchange via conduction and convection and the third one evaporative cooling by transpiration, quantifying the heat that is consumed by evaporation and drawn from the plant. The radiative and the evaporative terms are always positive whereas the conduction/convection term can change sign, transporting heat out of the plant if the leaf is warmer than the atmosphere and supplying heat to the leaf if it is cooler than the surroundings.

Leaf size is introduced into Equation E1 via the boundary layer thickness d_{bl} which depends on characteristic leaf length l_c via the (approximate) expression (Nobel, 2005)

$$d_{bl} = 4 \times 10^{-3}\,(\mathrm{m}/\sqrt{\mathrm{s}})\,\sqrt{l_c/v_w} \tag{E2}$$

Notice that Equation E1 connects leaf temperature T_l with l_c, implying that all three flux terms on the right hand side depend (at least implicitly) on l_c. It is important to realise that due to Equation E2 the conduction/convection flux decreases with increasing l_c, that is, its fraction of the flux balance is higher for small leaves than for large leaves.

Figure E1 illustrates these features for the location Svalbard for day 90 (close to spring equinox) in the morning (at 8 hr) and around midday (at 13 hr) and for two values of the atmospheric transmissivity ($\tau = 0.45$ and $\tau = 0.80$). Figure E2 does the same for day 185 (close to summer solstice). The upper rows of the figures show air temperature T_a (black) and leaf temperature T_l (magenta) as a function of leaf size and indicate thus the direction of the conduction/convection flux. The lower rows show the fluxes and their dependencies on characteristic leaf length l_c. The radiation absorbed by the leaf, represented by the left hand side of Equation E1, (black curves) should balance the right hand side of Equation E1, that is, radiation emanating from the leaf (red), heat exchange by conduction and convection (green) and evaporative heat loss due to transpiration (blue). Therefore, red, green and blue curve should add up to the black curve (which is obviously independent of leaf size) for all values of l_c.

- The radiation emanating from the leaf (red curve) balances 80%–90% of the incoming fluxes (black curve) whereas conduction/convection (green) and evaporation (blue) contribute much smaller fractions.
- For growing values of l_c, the green curve approaches—in accordance with Equation E2—the value zero, either from the positive side (for $T_l > T_a$, i.e., in case the leaf is warmer than the atmosphere) or from the negative side (if $T_l < T_a$). Since the red curve is only weakly dependent on l_c the blue curve has to bend into the opposite direction as the green curve (which is obviously the case) approaching for increasing l_c the value given by the difference between black and red curve. In other words: because the conduction/convection flux decreases with increasing l_c the evaporative heat loss has to fill the gap between incoming and outgoing radiation more and more alone.
- If the leaf is warmer than the atmosphere the conduction/convection flux has a positive sign (it points away from the leaf) and its decrease with increasing l_c induces the evaporation to increase. This applies in Figures E1 and E2

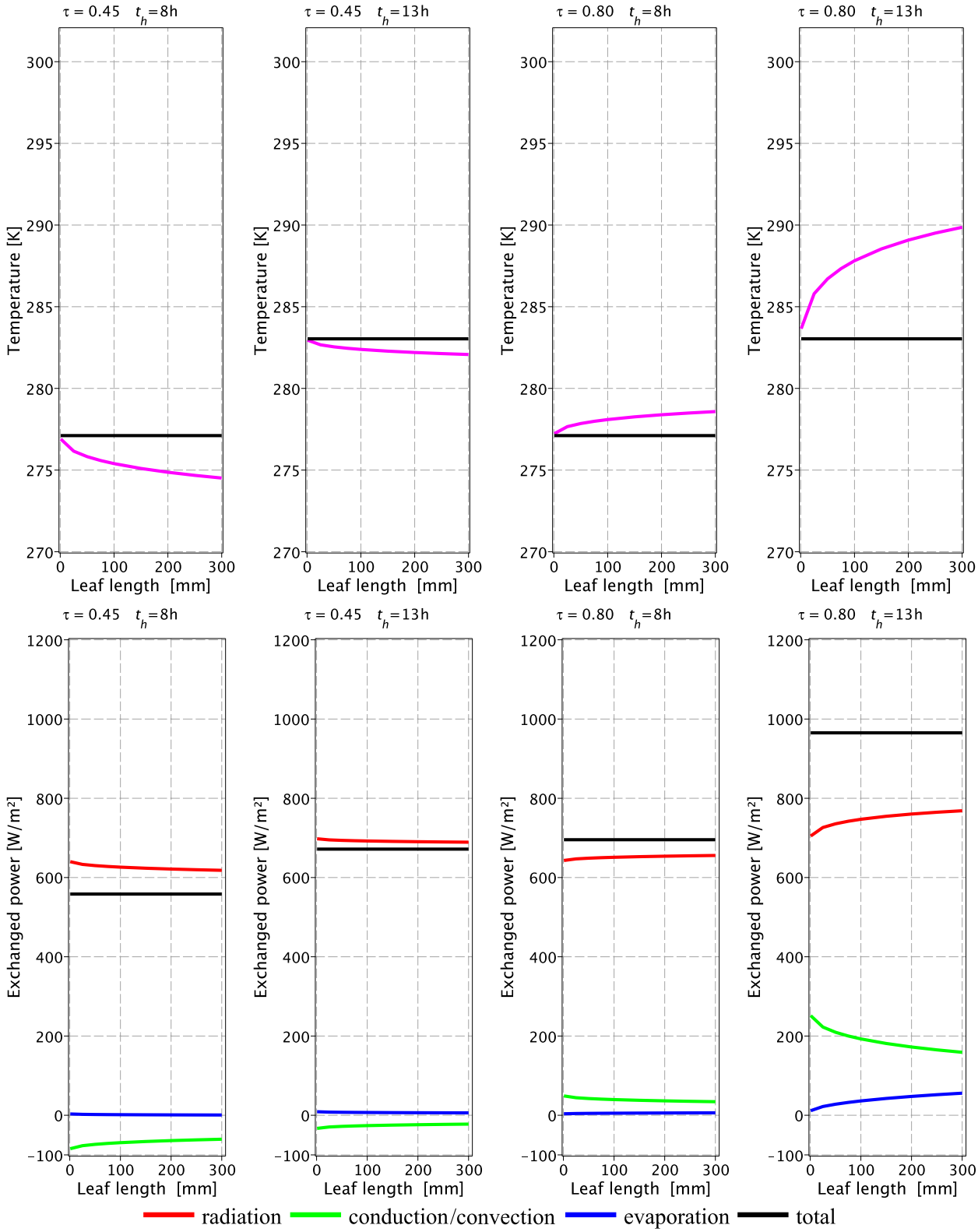

Figure E1. Upper row: Air temperature T_a (black) and leaf temperature T_l (magenta) as a function of characteristic leaf length l_c at day $d = 90$ at location Svalbard in the morning at $t = 8$ hr and close to midday at $t = 13$ hr and for two different values of atmospheric transmissivity ($\tau = 0.45$ and $\tau = 0.80$). Lower row: Energy exchange between leaf and environment. The radiation absorbed by the leaf, represented by the left hand side of Equation 2 (black curves), should balance the right hand side of Equation 2, that is, radiation emanating from the leaf (red), heat exchange by conduction and convection (green) and evaporative heat loss due to transpiration (blue). The leaf is oriented toward south and tilted against the horizontal by 45°. Atmospheric humidity and CO_2 are as given in Table 1, fraction of diffuse radiation is $k_d = 0.2$).

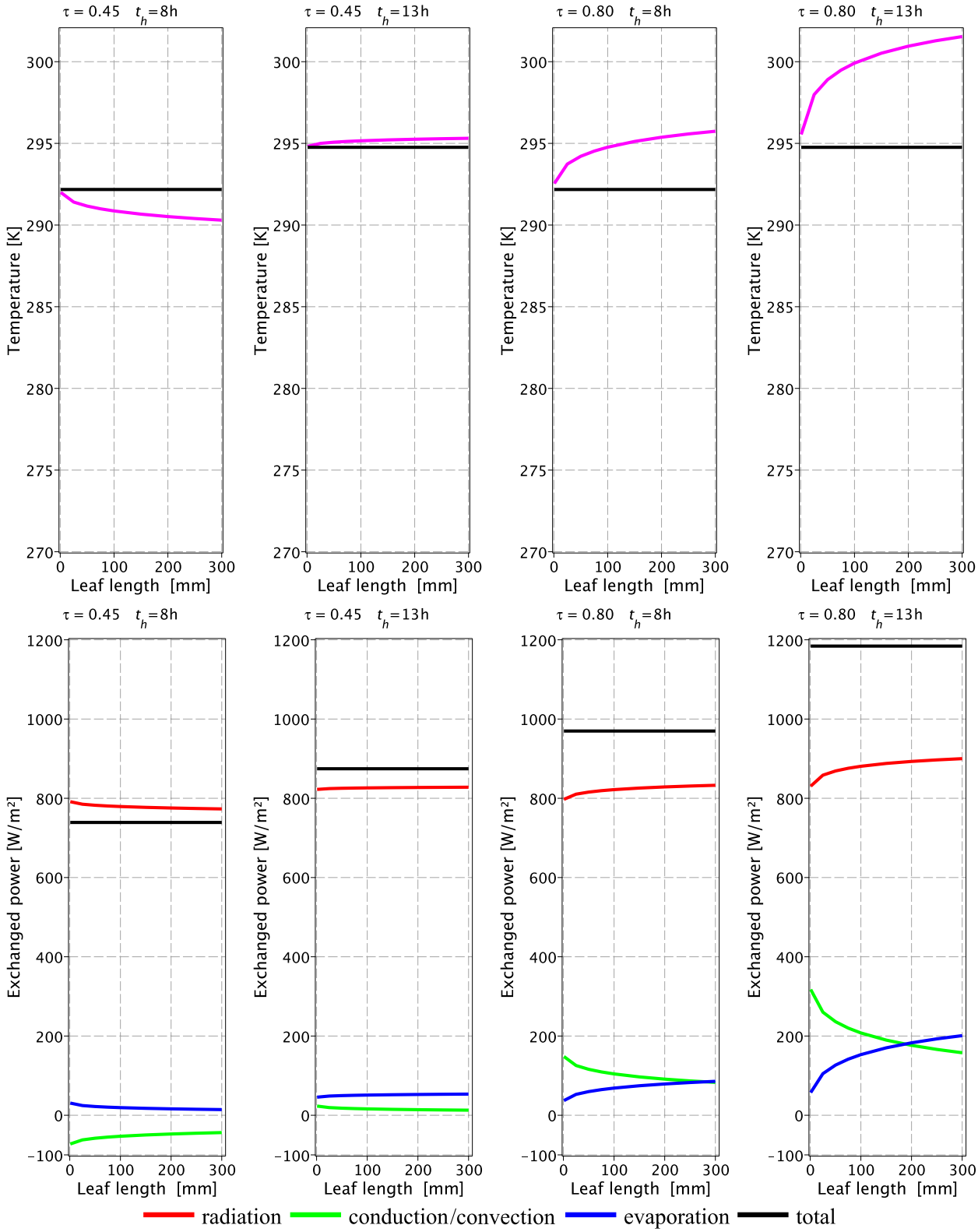

Figure E2. Upper row: Air temperature T_a (black) and leaf temperature T_l (magenta) as a function of characteristic leaf length l_c at day $d = 185$ at location Svalbard in the morning at $t = 8$ hr and close to midday at $t = 13$ hr and for two different values of atmospheric transmissivity ($\tau = 0.45$ and $\tau = 0.80$). Lower row: Energy exchange between leaf and environment. The radiation absorbed by the leaf, represented by the left hand side of Equation 2 (black curves), should balance the right hand side of Equation 2, that is, radiation emanating from the leaf (red), heat exchange by conduction and convection (green) and evaporative heat loss due to transpiration (blue). The leaf is oriented toward south and tilted against the horizontal by 45°. Atmospheric humidity and CO_2 are as given in Table 1, fraction of diffuse radiation is $k_d = 0.2$).

whenever the atmospheric transmissivity is high ($\tau = 0.80$) and for the not so clear ($\tau = 0.45$) summer day at noon (Figure E2). If the leaf is colder than the atmosphere, however, the conduction/convection flux has a negative sign (it points into the leaf) and its decrease with increasing l_c forces the evaporation to decrease, because otherwise the energy balance of the leaf would be violated. Provided the atmospheric transmissivity is low ($\tau = 0.45$), this occurs around the eqinoxes (Figure E1) and during summer in the morning (Figure E2).

- Decreasing evaporation means that transpiration and assimilation decrease also (they are both proportional to the leaf conductance g and therefore, according to the evaporation flux term in Equation E1, also to evaporation).

Summing up: if leaf irradiation is low, the complex physical interdependencies behind the balance Equation E1 effect that leaf temperature is lower than atmospheric temperature and the above reasoning explains why transpiration and assimilation decrease with increasing leaf size under low irradiation. The same reasoning explains also the converse case: under high irradiation large leaves are warmer than their surroundings and this is beneficial for transpiration and assimilation.

Appendix F: Sensitivity of Leaf Temperature and Assimilation Rate Against Variation of Leaf Orientation

The calculations of leaf temperature and assimilation presented as Figures 8 and 6 are restricted to leaves that are oriented toward South and tilted by 45° with respect to the horizontal ($H = 180°$ and $\Theta = 45°$ in the notation of Appendix A).

To estimate whether the results can be considered as representative also for other leaf orientations we calculated leaf temperatures and assimilation rates for other leaf angles and other directions with respect to celestial orientation, both for clear and overcast sky.

F1. Sensitivity of Leaf Temperature

By and large, the results for temperature, shown as Figure F1, are within the range of the results of Figure 8. Nonetheless a few details are remarkable:

- Under an overcast sky (lower row of Figure F1), the influence of leaf orientation on leaf temperature is negligible and leaf temperatures are always a few degrees lower than air temperature.
- In contrast, if sky is clear (upper row of Figure F1), the impact of leaf orientation on leaf temperature is considerable. Whether leaf temperature is above or below air temperature depends on leaf orientation (and confirms what one expects from the physics of the situation). The temperature of leaves with a horizontal lamina always exceeds air temperature; the temperature of inclined leaves, however, depends considerably on the cardinal direction—the difference in maximum leaf temperature between northerly and southerly oriented leaves (tilted by 45° with respect to the horizontal) amounts to about 10°C.

F2. Sensitivity of Assimilation Rate

The results for assimilation are presented as Figure F2. Notice that we calulated in this case the (instantaneous) assimilation rates at 13 hr instead of the annual assimilation shown in Figure 6.

For overcast sky (lower row of Figure F2), differences in assimilation rate caused by variation of leaf angle or cardinal point are hardly discernible. For clear sky (upper row of Figure F2), the impact of leaf orientation is slightly more meaningful.

Notice that at the beginning and at the end of the growing season assimilation rates are negative. This is due to the structure of Expression 5 (see also Appendix C) whose right hand side is the sum of a (positive) source term (representing the production of carbohydrates) and the (negative) sink term $-R_d$ which quantifies the mitochondrial respiration. The source term depends on both temperature and insolation, the sink term, however, only on temperature (for details, see Equation C6 in Appendix C). In spring and autumn, the interplay of temperature and insolation dependencies, driven by the growing (resp. declining) air temperature and solar insolation, results in an "outpacing" of assimilation by respiration, leading to short periods of negative net assimilation. According

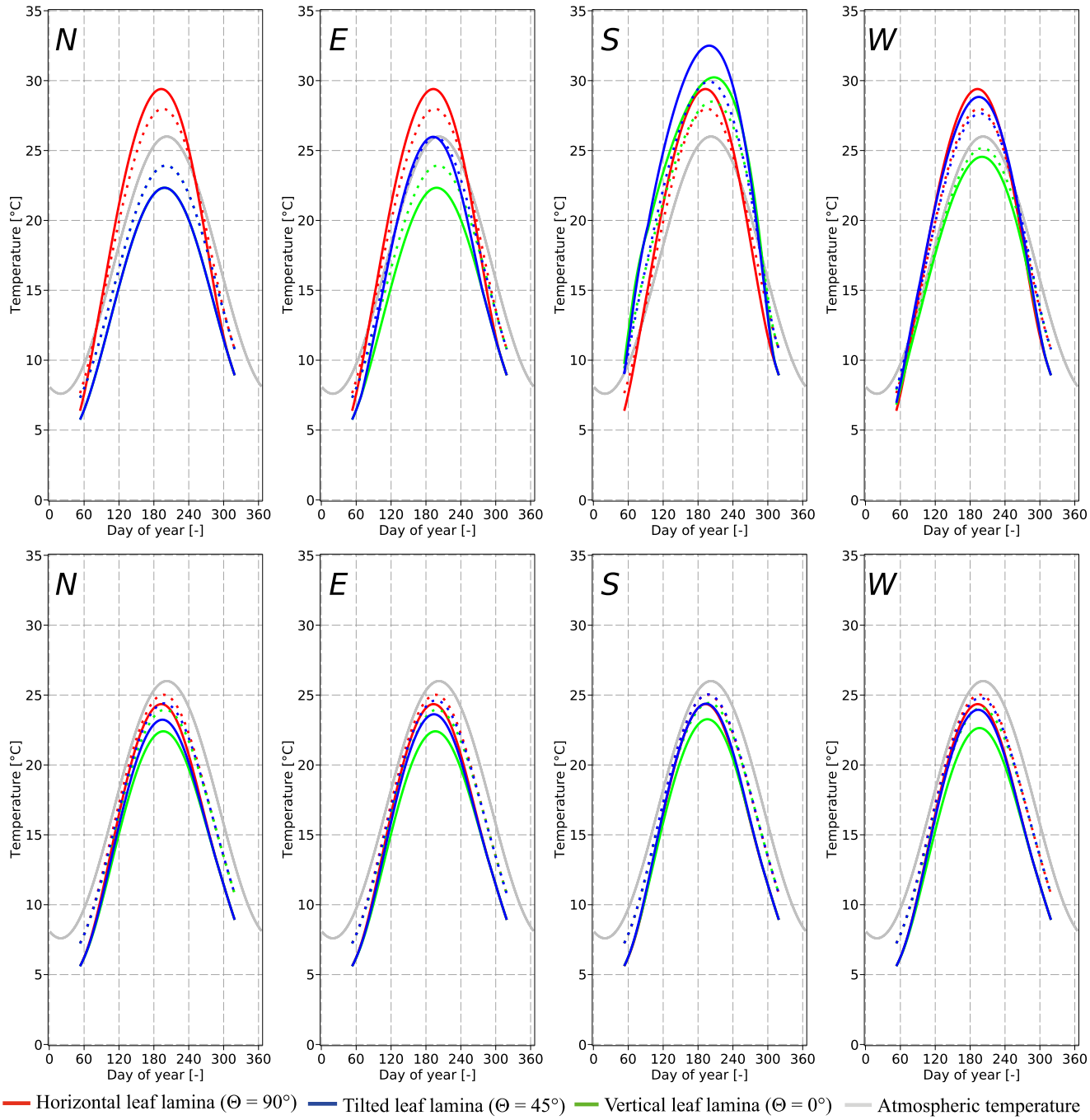

Figure F1. Variation of atmospheric temperature at 13 hr (solid gray curve) and leaf temperatures at 13 hr of smaller leaves ($l_c = 50$ mm, dotted lines) and larger leaves ($l_c = 250$ mm, solid lines) as a function of day of year at location Ellesmere Island. Leaves are oriented toward N (left column), E (second column), S (third column), or W (fourth column) and leaf normals are tilted against the horizontal by 0° (green curves), 45° (blue curves), or 90° (red curves). The upper row is related to clear skies ($k_d = 0.2$ and $\tau = 0.8$), the lower row refers to overcast skies ($k_d = 0.8$ and $\tau = 0.45$). In the upper left diagram, the green curves are identical with and covered by the blue curves. Similarly, in the diagram in the lower row showing temperatures for southerly oriented leaves under an overcast sky, the red curves are identical with and covered by the blue curves.

to Appendix C, assimilation rate depends on temperature and insolation in a rather complex way, effecting that source and sink term in Expression 5 may react on varying temperature and insolation in very different ways:

As illustrated by Figure 5, during early (phenological) autumn assimilation (the source term in Expression 5) decreases more rapidly than respiration (the sink), producing a negative assimilation rate.

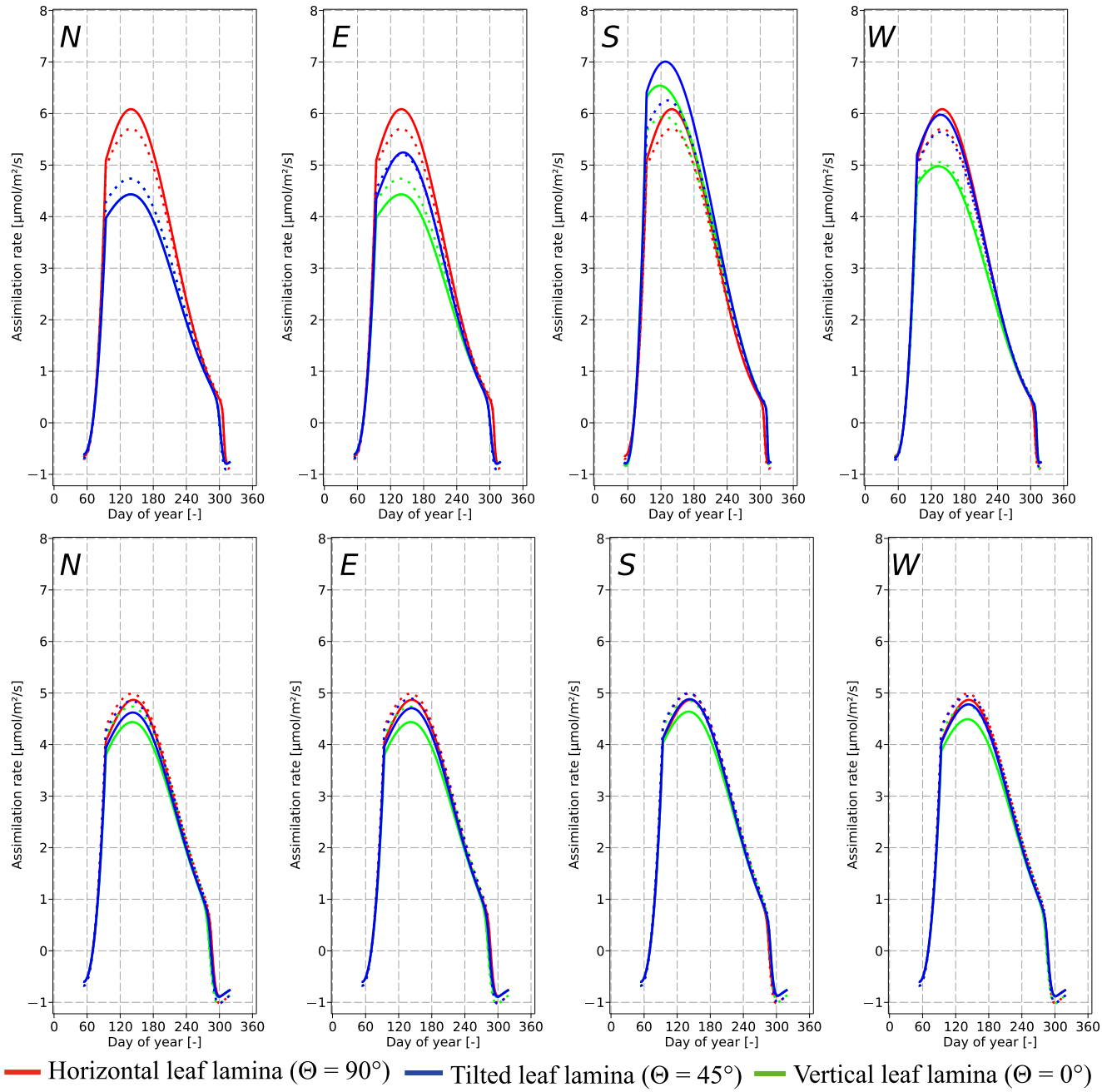

Figure F2. Variation of assimilation rate at 13 hr of smaller leaves ($l_c = 50$ mm, dotted lines) and larger leaves ($l_c = 250$ mm, solid lines) as a function of day of year at location Ellesmere Island. Leaves are oriented toward N (left column), E (second column), S (third column), or W (fourth column) and leaf normals are tilted against the horizontal by 0° (green curves), 45° (blue curves), or 90° (red curves). The upper row is related to clear skies ($k_d = 0.2$ and $\tau = 0.8$), the lower row refers to overcast skies ($k_d = 0.8$ and $\tau = 0.45$). In the upper left diagram, the green curves are identical with and covered by the blue curves. Similarly, in the diagram in the lower row showing temperatures for southerly oriented leaves under an overcast sky, the red curves are identical with and covered by the blue curves.

Shortly before the beginning of the polar night, however, the rates of assimilation and respiration adjust to new (daily changing) net results which are still negative, but slightly less negative than a few days before. This is illustrated by the small "hooks" of the assimilation curves shortly before the polar night (clearly discernible in the diagrams of the lower row of Figure F2).

Although the (instantaneous) assimilation rates shown in Figure F2 cannot be directly compared with the annual sums of assimilation of Figure 6, the similarity of the curves in Figure F2 suggests that the results presented in

Figure 6—calculated for southern direction and 45° leaf inclination only—are representative also for other leaf orientations.

Appendix G: Productivity of Modern Mid-Latitude Site (MMLS)

To evaluate the results of the canopy model, productivity data from the MODIS data base (Neumann et al., 2016) for the immediate surroundings of the MMLS were used. In Figure G1, the grid cells showing these data are depicted in the upper image by reddish boxes. The scale showing the productivity values is included in the figure. To obtain productivity values for deciduous broad leaved trees, only areas covered by hardwood forest were selected. These were identified by using the Corine Land Cover Data (https://land.copernicus.eu/pan-european/corine-land-cover/clc2018) and indicated by black spots on the lower image (Figure G1).

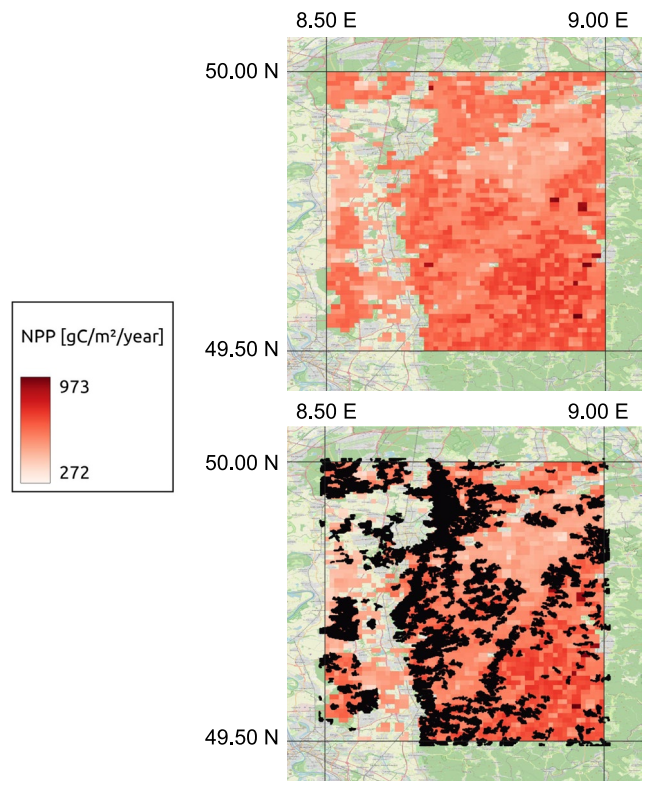

Figure G1. Productivity data for a 0.5° × 0.5° latitude/longitude grid cell including the present-day mid-latitude site MMLS with center coordinates (49.75°/8.75°) (New et al., 1999); red grid cells represent NPP grid cells with 1 × 1 km resolution (Neumann et al., 2016); black dots indicate grid points covered by broad leaf decidious forest according to Corine Land Cover Data.

Data Availability Statement

The data on which this article is based are available in van Hinsbergen et al. (2015); West et al. (2015); Uhl et al. (2007); New et al. (1999); Kosugi et al. (2003); Lalic and Mihailovic (2004) and Lalic et al. (2013). The model itself is a straightforward application of the equations presented in Section 3.1 and in Appendices A to D. For the actual calculations the computer algebra system `maple` (Maplesoft, 2022) has been used, details are described in Section 3.7. Maple sheets for the calculation of annual assimilation and transpiration sums as a function of characteristic leaf length and CO_2 (Konrad, 2023) have been deposited in the FDAT-repository of the University of Tübingen (Konrad, 2023) [Creative Commons Attribution 4.0 International license].

The Modis NPP data, including the link ftp://palantir.boku.ac.at/Public/MODIS_EURO, can be found in (Neumann et al., 2016). The land cover data are on the Copernicus website https://land.copernicus.eu/pan-european/corine-land-cover/clc2018.

Acknowledgments
We thank James Nebelsick, University of Tübingen, for critically reading the English manuscript. Open Access funding enabled and organized by Projekt DEAL.

References

Ainsworth, E. A., & Long, S. P. (2005). What have we learned from 15 years of free-air CO_2 enrichment (FACE)? A meta-analytic review of the responses of photosynthesis, canopy properties and plant production to rising CO_2. *New Phytologist*, *165*(2), 351–372. https://doi.org/10.1111/j.1469-8137.2004.01224.x

Anagnostou, E., John, E. H., Edgar, K. M., Foster, G. L., Ridgwell, A., Inglis, G. N., et al. (2016). Changing atmospheric CO_2 concentration was the primary driver of early Cenozoic climate. *Nature*, *533*, 380–384.

Bader, M. K.-F., Leuzinger, S., Keel, S. G., Siegwolf, R. T. W., Hagedorn, F., Schleppi, P., & Körner, C. (2013). Central European hardwood trees in a high-CO_2 future: Synthesis of an 8-year forest canopy CO_2 enrichment project. *Journal of Ecology*, *101*(6), 1509–1519. https://doi.org/10.1111/1365-2745.12149

Bader, M. K.-F., Siegwolf, R., & Körner, C. (2010). Sustained enhancement of photosynthesis in mature deciduous forest trees after 8 years of free air CO_2 enrichment. *Planta*, *232*(5), 1115–1125. https://doi.org/10.1007/s00425-010-1240-8

Basinger, J. F., Greenwood, D. R., & Sweda, T. (1994). Early tertiary vegetation of Arctic Canada and its relevance to paleoclimatic interpretation. In *Cenozoic plants and climates of the Arctic* (pp. 175–198). Springer.

Bernacchi, C. J., Pimentel, C., & Long, S. P. (2003). Vivo temperature response functions of parameters required to model RuBP-limited photosynthesis. *Plant, Cell and Environment*, *26*(9), 1419–1430. https://doi.org/10.1046/j.0016-8025.2003.01050.x

Budantsev, L. Y. (1983). *Istoria arkticeskoj flory epochi rannego kajnofita. (the early cenophytic history of the Arctic flora)*. Nauka.

Burke, K. D., Williams, J. W., Chandler, M. A., Haywood, A., Lunt, D. J., & Otto-Bliesner, B. L. (2018). Pliocene and Eocene provide best analogs for near-future climates. *Proceedings of the National Academy of Sciences*, *115*(52), 13288–13293. https://doi.org/10.1073/pnas.1809600115

Cleveland, C. C., Townsend, A. R., Taylor, P., Alvarez-Clare, S., Bustamante, M. M., Chuyong, G., et al. (2011). Relationships among net primary productivity, nutrients and climate in tropical rain forest: A pan-tropical analysis. *Ecology Letters*, *14*(9), 939–947. https://doi.org/10.1111/j.1461-0248.2011.01658.x

Collinson, M. E., & Hooker, J. J. (2003). Paleogene vegetation of eurasia: Framework for mammalian faunas. *Deinsea*, *10*, 41–83.

Crabaugh, J. P., & Steel, R. J. (2004). Basin-floor fans of the Central Tertiary Basin, Spitsbergen: Relationship of basin-floor sand-bodies to prograding clinoforms in a structurally active basin. *Geological Society, London, Special Publications*, *222*(1), 187–208. https://doi.org/10.1144/gsl.sp.2004.222.01.10

Cunningham, S. A., Summerhayes, B., & Westoby, M. (1999). Evolutionary divergences in leaf structure and chemistry, comparing rainfall and soil nutrient gradients. *Ecological Monographs*, *69*(4), 569–588. https://doi.org/10.1890/0012-9615(1999)069[0569:edilsa]2.0.co;2

Dolph, G. E., & Dilcher, D. L. (1980). Variation in leaf size with respect to climate in the tropics of the western hemisphere. *Bulletin of the Torrey Botanical Club*, *107*(2), 154–162. https://doi.org/10.2307/2484220

Dong, N., Wright, I. J., Chen, J. M., Luo, X., Wang, H., Keenan, T. F., et al. (2022). Rising CO_2 and warming reduce global canopy demand for nitrogen. *New Phytologist*, *235*(5), 1692–1700. https://doi.org/10.1111/nph.18076

Eberle, J. J., & Greenwood, D. R. (2012). Life at the top of the greenhouse Eocene world–A review of the Eocene flora and vertebrate fauna from Canada's High Arctic. *Geological Society of America Bulletin*, *124*(1–2), 3–23. https://doi.org/10.1130/b30571.1

Eldrett, J. S., Greenwood, D. R., Harding, I. C., & Huber, M. (2009). Increased seasonality through the Eocene to Oligocene transition in northern high latitudes. *Nature*, *459*(7249), 969–973. https://doi.org/10.1038/nature08069

Farquhar, G. D., von Caemmerer, S., & Berry, J. A. (1980). A biochemical model of photosynthetic CO_2 assimilation in leaves of C_3 species. *Planta*, *149*(1), 78–90. https://doi.org/10.1007/bf00386231

Farquhar, G. D., Von Caemmerer, S., & Berry, J. A. (2001). Models of photosynthesis. *Plant Physiology*, *125*(1), 42–45. https://doi.org/10.1104/pp.125.1.42

Foster, G. L., Royer, D. L., & Lunt, D. J. (2017). Future climate forcing potentially without precedent in the last 420 million years. *Nature Communications*, *8*(1), 14845. https://doi.org/10.1038/ncomms14845

Francis, J. E. (1988). A 50-million-year-old fossil forest from Strathcona Fiord, Ellesmere Island, Arctic Canada: Evidence for a warm polar climate. *Arctic*, *41*(4), 314–318. https://doi.org/10.14430/arctic1738

Francis, J. E. (1991). Tertiary fossil forests of the Geodetic Hills, Axel Heiberg Island, Arctic Archipelago. *Geological Survey of Canada Bulletin*, *403*, 29–38.

Frank, C. W., Wahl, S., Keller, J. D., Pospichal, B., Hense, A., & Crewell, S. (2018). Bias correction of a novel european reanalysis data set for solar energy applications. *Solar Energy*, *164*, 12–24. https://doi.org/10.1016/j.solener.2018.02.012

Golovneva, L. B. (2000a). Early Palaeogene floras of Spitsbergen and North Atlantic floristic exchange. *Acta Universitatis Carolinae: Geologica*, *44*(1), 39–50.

Golovneva, L. B. (2000b). Palaeogene climates of Spitsbergen. *GFF (Geological Society of Sweden)*, *122*(1), 62–63. https://doi.org/10.1080/11035890001221062

Greenwood, D. R., & Basinger, J. F. (1994). The paleoecology of high-latitude Eocene swamp forests from Axel Heiberg Island, Canadian High Arctic. *Review of Palaeobotany and Palynology*, *81*(1), 83–97. https://doi.org/10.1016/0034-6667(94)90128-7

Greenwood, D. R., Basinger, J. F., & Smith, R. Y. (2010). How wet was the Arctic Eocene rain forest? Estimates of precipitation from Paleogene Arctic macrofloras. *Geology*, *38*(1), 15–18. https://doi.org/10.1130/g30218.1

Hamada, S., Kumagai, T., Kochi, K., Kobayashi, N., Hiyama, T., & Miyazawa, Y. (2016). Spatial and temporal variations in photosynthetic capacity of a temperate deciduous-evergreen forest. *Trees*, *30*(4), 1083–1093. https://doi.org/10.1007/s00468-015-1347-4

Harrington, G. J., Eberle, J., Le-Page, B. A., Dawson, M., & Hutchison, J. H. (2011). Arctic plant diversity in the Early Eocene greenhouse. *Proceedings of the Royal Society B*, *279*(1733), 1–7. https://doi.org/10.1098/rspb.2011.1704

Harrison, D. L., Bates, P. J. J., Pearch, M., Michaels, C., & Ward, D. J. (2012). New additions to the late middle Eocene mammal fauna of Creechbarrow, Dorset, southern England. *Cainozoic Research*, *9*(1), 65–85.

Heer, O. (1859). *Die tertiäre Flora der Schweiz (Flora tertiaria Helvetiae)* (Vol. 3). J. Wurster-Comp.

Heer, O. (1868). Flora fossilis Arctica - Die fossile flora der Polarländer. (Vol. Band *1*, pp. 1–192).

Huber, M., & Goldner, A. (2012). Eocene monsoons. *Journal of Asian Earth Sciences*, *44*, 3–23. https://doi.org/10.1016/j.jseaes.2011.09.014

Jagniecki, E. A., Lowenstein, T. K., Jenkins, D. M., & Demicco, R. V. (2015). Eocene atmospheric CO_2 from the nahcolite proxy. *Geology*, *43*(12), 1075–1078. https://doi.org/10.1130/g36886.1

Jahren, A. H., & Sternberg, L. S. L. (2003). Humidity estimate for the middle Eocene Arctic rain forest. *Geology*, *31*(5), 463–466. https://doi.org/10.1130/0091-7613(2003)031<0463:heftme>2.0.co;2

Kikuzawa, K., & Lechowicz, M. J. (2011). *Ecology of leaf longevity*. Springer. https://doi.org/10.1007/978-4-431-53918-6

Konrad, W. (2023). Maple sheets for the calculation of annual assimilation and transpiration sums as a function of characteristic leaf length and CO_2. [Software]. University of Tübingen. https://doi.org/10.57754/FDAT.jb0nw-xx142

Konrad, W., Katul, G., & Roth-Nebelsick, A. (2020). Leaf temperature and its dependence on atmospheric CO_2 and leaf size. *Geological Journal*, *56*(2), 866–885. https://doi.org/10.1002/gj.3757

Konrad, W., Katul, G., Roth-Nebelsick, A., & Grein, M. (2017). A reduced order model to analytically infer atmospheric CO_2 concentration from stomatal and climate data. *Advances in Water Resources*, *104*, 145–157. https://doi.org/10.1016/j.advwatres.2017.03.018

Körner, C. (2006). Plant CO_2 responses: An issue of definition, time and resource supply. *New Phytologist*, *172*(3), 393–411. https://doi.org/10.1111/j.1469-8137.2006.01886.x

Kosugi, Y., Shibata, S., & Kobashi, S. (2003). Parameterization of the CO_2 and H_2O gas exchange of several temperate deciduous broad-leaved trees at the leaf scale considering seasonal changes. *Plant, Cell and Environment*, *26*(2), 285–301. https://doi.org/10.1046/j.1365-3040.2003.00960.x

Kotyk, M. E. A., Basinger, J. F., & McIver, E. E. (2003). Early tertiary *Chamaecyparis* Spach from Axel Heiberg Island, Canadian High Arctic. *Canadian Journal of Botany*, *81*(2), 113–130. https://doi.org/10.1139/b03-007

Kvaček, Z. (2010). Forest flora and vegetation of the European early Palaeogene—A review. *Bulletin of Geosciences*, *85*(1), 3–16. https://doi.org/10.3140/bull.geosci.1146

Kvaček, Z., Manum, S. B., & Boulter, M. C. (1994). Angiosperms from the Palaeogene of Spitsbergen, including an unfinished work by A.G. Nathorst. Palaeontographica. *Abteilung B*, *232*, 103–128.

Lalic, B., Firanj, A., Mihailovic, D. T., & Podrascanin, Z. (2013). Parameterization of PAR vertical profile within horizontally uniform forest canopies for use in environmental modeling. *Journal of Geophysical Research: Atmospheres*, *118*(15), 8156–8165. https://doi.org/10.1002/jgrd.50626

Lalic, B., & Mihailovic, D. T. (2004). An empirical relation describing leaf-area density inside the forest for environmental modeling. *Journal of Applied Meteorology*, *43*(4), 641–645. https://doi.org/10.1175/1520-0450(2004)043<0641:aerdld>2.0.co;2

Larcher, W. (2003). *Physiological plant ecology: Ecophysiology and stress physiology of functional groups*. Springer Science & Business Media.

LePage, B. A. (2001). New species of *Picea* A. Dietrich (Pinaceae) from the middle eocene of Axel Heiberg Island, Arctic Canada. *Botanical Journal of the Linnean Society*, *135*(2), 137–167. https://doi.org/10.1111/j.1095-8339.2001.tb01088.x

LePage, B. A. (2003). A new species of *Tsuga* (Pinaceae) from the middle Eocene of Axel Heiberg Island, Canada, and an assessment of the evolution and biogeographical history of the genus. *Botanical Journal of the Linnean Society*, *141*(3), 257–296. https://doi.org/10.1046/j.1095-8339.2003.00131.x

Liu, B. Y. H., & Jordan, R. C. (1960). The interrelationship and characteristic distribution of direct, diffuse and total solar radiation. *Solar Energy*, *4*(3), 1–19. https://doi.org/10.1016/0038-092x(60)90062-1

Loutzenhiser, P. G., Manz, H., Felsmann, C., Strachan, P. A., Frank, T., & Maxwell, G. M. (2007). Empirical validation of models to compute solar irradiance on inclined surfaces for building energy simulation. *Solar Energy*, *81*(2), 254–267. https://doi.org/10.1016/j.solener.2006.03.009

Manum, S. B., & Throndsen, T. (1986). Age of tertiary formations on Spitsbergen. *Polar Research*, *4*(2), 103–131. https://doi.org/10.3402/polar.v4i2.6927

Maplesoft. (2022). Maple [Software]. Maplesoft is a division of Waterloo Maple Inc. Retrieved from https://www.maplesoft.com/

McDonald, P., Fonseca, C., McC, J., & Westoby, M. (2003). Leaf-size divergence along rainfall and soil-nutrient gradients: Is the method of size reduction common among clades? *Functional Ecology*, *17*(1), 50–57. https://doi.org/10.1046/j.1365-2435.2003.00698.x

McIver, E. E., & Basinger, J. F. (1999). Early tertiary floral evolution in the Canadian High Arctic. *Annals of the Missouri Botanical Garden*, *86*(2), 523. https://doi.org/10.2307/2666184

Monteith, J., & Unsworth, M. H. (2013). *Principles of environmental physics*. Elsevier LTD.

Nathorst, A. G. (1915). Tertiäre Pflanzenreste aus Ellesmere-land. In: *Reports of the second Norwegian Arctic expedition in the "Fram" 35: 1898–1902*.

Neumann, M., Moreno, A., Thurnher, C., Mues, V., Härkönen, S., Mura, M., et al. (2016). Creating a regional modis satellite-driven net primary production dataset for european forests. *Remote Sensing*, *8*(7), 554. https://doi.org/10.3390/rs8070554

New, M., Hulme, M., & Jones, P. (1999). Representing twentieth-century space-time climate variability. Part I: Development of a 1961-90 mean monthly terrestrial climatology. *Journal of Climate*, *12*(3), 829–856. https://doi.org/10.1175/1520-0442(1999)012<0829:rtcstc>2.0.co;2

Nobel, P. S. (2005). *Physicochemical and environmental plant physiology* (3rd ed.). Elsevier Academic Press.

Norby, R. J., Warren, J. M., Iversen, C. M., Childs, J., Jawdy, S. S., & Walker, A. P. (2022). Forest stand and canopy development unaltered by 12 years of CO_2 enrichment. *Tree Physiology*, *42*(3), 428–440. https://doi.org/10.1093/treephys/tpab107

Prescott, C. E., Grayston, S. J., Helmisaari, H.-S., Kaštovská, E., Körner, C., Lambers, H., et al. (2020). Surplus carbon drives allocation and plant–soil interactions. *Trends in Ecology & Evolution*, *35*(12), 1110–1118. https://doi.org/10.1016/j.tree.2020.08.007

Reichgelt, T., Greenwood, D. R., Steinig, S., Conran, J. G., Hutchinson, D. K., Lunt, D. J., et al. (2022). Plant proxy evidence for high rainfall and productivity in the Eocene of Australia. *Paleoceanography and Paleoclimatology*, *37*(6), e2022PA004418. https://doi.org/10.1029/2022pa004418

Reif, F. (1974). *Fundamentals of statistical and thermal physics*. McGraw-Hill.

Reinhardt, L., Estrada, S., Andruleit, H., Dohrmann, R., Piepjohn, K., von Gosen, W., et al. (2013). Altered volcanic ashes in Palaeocene and Eocene sediments of the Eureka Sound Group (Ellesmere Island, Nunavut, Arctic Canada). *Zeitschrift der Deutschen Gesellschaft für Geowissenschaften*, *164*(1), 131–147. https://doi.org/10.1127/1860-1804/2013/0004

Royer, D. L., Osborne, C. P., & Beerling, D. J. (2005). Contrasting seasonal patterns of carbon gain in evergreen and deciduous trees of ancient polar forests. *Paleobiology*, *31*(1), 141–150. https://doi.org/10.1666/0094-8373(2005)031<0141:cspocg>2.0.co;2

Schei, P. (1903). Summary of geological results. *The Geographical Journal*, *22*(1), 56–65. https://doi.org/10.2307/1775049

Schuepp, P. H. (1993). Tansley review no. 59 leaf boundary layers. *New Phytologist*, *125*(3), 477–507. https://doi.org/10.1111/j.1469-8137.1993.tb03898.x

Steinthorsdottir, M., Vajda, V., Pole, M., & Holdgate, G. (2019). Moderate levels of Eocene pCO_2 indicated by Southern Hemisphere fossil plant stomata. *Geology*, *47*(10), 914–918. https://doi.org/10.1130/g46274.1

Sunderlin, D., Loope, G., Parker, N. E., & Williams, C. J. (2011). Paleoclimatic and paleoecological implications of a Paleocene–Eocene fossil leaf assemblage, chickaloon formation, Alaska. *PALAIOS*, *26*(6), 335–345. https://doi.org/10.2110/palo.2010.p10-077r

Turner, D. P., Ritts, W. D., Cohen, W. B., Gower, S. T., Running, S. W., Zhao, M., et al. (2006). Evaluation of modis NPP and GPP products across multiple biomes. *Remote Sensing of Environment*, *102*(3–4), 282–292. https://doi.org/10.1016/j.rse.2006.02.017

Uhl, D., Traiser, C., Griesser, U., & Denk, T. (2007). Fossil leaves as palaeoclimate proxies in the Palaeogene of Spitsbergen (Svalbard). *Acta Palaeobotanica*, *47*, 89–107.

van Hinsbergen, D. J. J., de Groot, L. V., van Schaik, S. J., Spakman, W., Bijl, P. K., Sluijs, A., et al. (2015). A paleolatitude calculator for paleoclimate studies. *PLoS One*, *10*(6), e0126946. https://doi.org/10.1371/journal.pone.0126946

Vinod, N., Slot, M., McGregor, I. R., Ordway, E. M., Smith, M. N., Taylor, T. C., et al. (2022). Thermal sensitivity across forest vertical profiles: Patterns, mechanisms, and ecological implications. *New Phytologist*, *237*(1), 22–47. https://doi.org/10.1111/nph.18539

Wappler, T., & Denk, T. (2011). Herbivory in early tertiary Arctic forests. *Palaeogeography, Palaeoclimatology, Palaeoecology*, *310*(3–4), 283–295. https://doi.org/10.1016/j.palaeo.2011.07.020

West, C. K., Greenwood, D. R., & Basinger, J. F. (2015). Was the Arctic Eocene 'rainforest' monsoonal? Estimates of seasonal precipitation from early Eocene megafloras from Ellesmere Island, Nunavut. *Earth and Planetary Science Letters*, *427*, 18–30. https://doi.org/10.1016/j.epsl.2015.06.036

West, C. K., Greenwood, D. R., & Basinger, J. F. (2019). The late Paleocene to early Eocene Arctic megaflora of Ellesmere and Axel Heiberg islands, Nunavut, Canada. *Palaeontographica Abteilung B*, *300*(1–6), 47–163. https://doi.org/10.1127/palb/2019/0066

West, C. K., Greenwood, D. R., Reichgelt, T., Lowe, A. J., Vachon, J. M., & Basinger, J. F. (2020). Paleobotanical proxies for early Eocene climates and ecosystems in northern North America from middle to high latitudes. *Climate of the Past*, *16*(4), 1387–1410. https://doi.org/10.5194/cp-16-1387-2020

Wilf, P., Wing, S. L., Greenwood, D. R., & Greenwood, C. L. (1998). Using fossil leaves as paleoprecipitation indicators: An Eocene example. *Geology*, *26*(3), 203–206. https://doi.org/10.1130/0091-7613(1998)026<0203:uflapi>2.3.co;2

Willard, D. A., Donders, T. H., Reichgelt, T., Greenwood, D. R., Sangiorgi, F., Peterse, F., et al. (2019). Arctic vegetation, temperature, and hydrology during early Eocene transient global warming events. *Global and Planetary Change*, *178*, 139–152. https://doi.org/10.1016/j.gloplacha.2019.04.012

Williams, C. J., Johnson, A. H., LePage, B. A., Vann, D. R., & Sweda, T. (2003). Reconstruction of Tertiary Metasequoia forests. II. Structure, biomass, and productivity of Eocene floodplain forests in the Canadian Arctic. *Paleobiology*, *29*(2), 271–292. https://doi.org/10.1666/0094-8373(2003)029⟨0271:ROTMFI⟩2.0.CO;2

Williams, C. J., Mendell, E. K., Murphy, J., Court, W. M., Johnson, A. H., & Richter, S. L. (2008). Paleoenvironmental reconstruction of a Middle Miocene forest from the western Canadian Arctic. *Palaeogeography, Palaeoclimatology, Palaeoecology*, *261*(1–2), 160–176. https://doi.org/10.1016/j.palaeo.2008.01.014

Wilson, K. B., Baldocchi, D. D., & Hanson, P. J. (2000). Spatial and seasonal variability of photosynthetic parameters and their relationship to leaf nitrogen in a deciduous forest. *Tree Physiology*, *20*(9), 565–578. https://doi.org/10.1093/treephys/20.9.565

Wolfe, J. A. (1985). Distribution of major vegetational types during the tertiary. *Geophysical Monograph Series American Geophysical Union*, *32*, 357–375.

Wright, I. J., Dong, N., Maire, V., Prentice, I. C., Westoby, M., Díaz, S., et al. (2017). Global climatic drivers of leaf size. *Science*, *357*(6354), 917–921. https://doi.org/10.1126/science.aal4760

Xu, L., & Baldocchi, D. D. (2003). Seasonal trends in photosynthetic parameters and stomatal conductance of blue oak (*Quercus douglasii*) under prolonged summer drought and high temperature. *Tree Physiology*, *23*(13), 865–877. https://doi.org/10.1093/treephys/23.13.865

Zhao, M., Heinsch, F. A., Nemani, R. R., & Running, S. W. (2005). Improvements of the modis terrestrial gross and net primary production global data set. *Remote Sensing of Environment*, *95*(2), 164–176. https://doi.org/10.1016/j.rse.2004.12.011